Production of K^+ and of K^- mesons in heavy-ion collisions from 0.6A to 2.0A GeV incident energy

A. Förster,[2,*] F. Uhlig,[1,2] I. Böttcher,[4] D. Brill,[1] M. Dębowski,[5,6] F. Dohrmann,[6] E. Grosse,[6,7] P. Koczoń,[1] B. Kohlmeyer,[4] S. Lang,[1,2] F. Laue,[1,†] M. Mang,[1] M. Menzel,[4] C. Müntz,[1,2,3] L. Naumann,[6] H. Oeschler,[2] M. Płoskoń,[1,3] W. Scheinast,[6] A. Schmah,[1,2] T. J. Schuck,[3,*] E. Schwab,[1] P. Senger,[1] Y. Shin,[3] J. Speer,[1,‡] H. Ströbele,[3] C. Sturm,[1,2,3] G. Surówka,[1,5] A. Wagner,[2,6] and W. Waluś[5]

(KaoS Collaboration)

[1]*Gesellschaft für Schwerionenforschung, D-64220 Darmstadt, Germany*
[2]*Technische Universität Darmstadt, D-64289 Darmstadt, Germany*
[3]*Johann Wolfgang Goethe-Universität, D-60325 Frankfurt am Main, Germany*
[4]*Phillips-Universität, D-35037 Marburg, Germany*
[5]*Uniwersytet Jagielloński, PL-30059 Kraków, Poland*
[6]*Forschungszentrum Dresden-Rossendorf, D-01314 Dresden, Germany*
[7]*Technische Universität Dresden, D-01062 Dresden, Germany*

(Received 30 August 2006; published 22 February 2007)

This paper summarizes the yields and the emission patterns of K^+ and of K^- mesons measured in inclusive C+C, Ni+Ni, and Au+Au collisions at incident energies from 0.6A to 2.0A GeV using the Kaon Spectrometer KaoS at GSI. For Ni+Ni collisions at 1.5A and at 1.93A GeV as well as for Au+Au at 1.5A GeV, detailed results are presented of the multiplicities, of the inverse slope parameters, and of the anisotropies in the angular emission patterns as a function of the collision centrality. When comparing transport-model calculations to the measured K^+ production yields, an agreement is only obtained for a soft nuclear equation of state (compression modulus $K_N \approx 200$ MeV). The production of K^- mesons at energies around 1A to 2A GeV is dominated by the strangeness-exchange reaction $K^-N \rightleftharpoons \pi Y$ ($Y = \Lambda, \Sigma$) which leads to a coupling between the K^- and K^+ yields. However, both particle species show distinct differences in their emission patterns suggesting different freeze-out conditions for K^+ and K^- mesons.

DOI: 10.1103/PhysRevC.75.024906 PACS number(s): 25.75.Dw

I. INTRODUCTION

Relativistic heavy-ion collisions at incident energies ranging from 0.6A to 2.0A GeV provide a unique opportunity to study the behavior of nuclear matter at high densities. These studies are important challenges for testing the present understanding of nuclear matter. In addition, they are of relevance to astrophysics, as the modeling of neutron stars or supernovas depends on the properties of nuclear matter under these extreme conditions [1].

In central Au+Au collisions at the incident energies under investigation, densities of 2–3 times normal nuclear matter density can be reached [2–4]. A sensitive probe to test these conditions is the production of strange mesons at or below the production thresholds of these particles in free NN collisions. The rest mass of charged kaons is 0.454 GeV. For the K^+ production, the threshold in NN collisions is 1.58 GeV (in the laboratory system) as defined by the associate production $NN \rightarrow K^+\Lambda N$, and it is 2.5 GeV for the K^- production via pair creation $NN \rightarrow NNK^-K^+$.

The key mechanism for the K^+ production in heavy-ion reactions at these incident energies is the accumulation of the necessary energy by multiple collisions of particles inside the reaction zone. Higher densities increase the number of these collisions, and especially second-generation collisions such as ΔN with sufficiently high relative momentum to create a K^+ occur most frequently during the high-density phase of the reaction. The density reached in the reaction zone depends on the stiffness of nuclear matter. Because of their specific production mechanism and because of their rather long mean free path ($\approx$5 fm at normal nuclear density), K^+ mesons are ideal probes for exploring the high-density phase of a heavy-ion reaction and for studying the stiffness of the nuclear equation of state (EoS) [5–9].

In contrast, the behavior of K^- mesons in a dense nuclear medium is expected to be very different from the one of the K^+ mesons because of two distinct properties:

(i) The interaction with nuclear matter: The K^+ are hardly absorbed in nuclear matter due to strangeness conservation. It is very unlikely that a rare K^+ (containing an $\bar{s}$ quark) encounters an equally rare hyperon Y (Λ, Σ) containing an s quark. The K^-, on the contrary, can easily be absorbed on a nucleon, converting it into a hyperon and a pion. Consequently, the mean free path of the K^- is significantly shorter than the one of the K^+. The strangeness-exchange reaction $K^-N \rightleftharpoons \pi Y$ has a large cross section and is therefore responsible for the appearance and disappearance of K^- mesons. It has been suggested that this channel is the dominant production mechanism in nucleus-nucleus collisions [5], and this has been demonstrated in Refs. [10–12].

*Present address: Max-Planck-Institut für Kernphysik, D-69117 Heidelberg, Germany
†Present address: Brookhaven National Laboratory, Upton, New York 11973, USA
‡Deceased

 ©2007 The American Physical Society

(ii) The influence of *KN* potentials: According to various theoretical approaches, the *KN* interaction is governed by the superposition of a scalar and a vector potential [13–18]. While the scalar potential acts attractively on both kaon species, the vector potential repels K^+ and attracts K^-. For K^+, these two contributions almost cancel, leading to a small repulsive K^+N interaction. For K^-, the addition of both attractive interactions results in a strongly attractive potential. Attempts to observe these effects in the respective production cross sections are under discussion [12,19–24]. These potentials are predicted to have a sizable effect on the azimuthal emission patterns of K^+ and of K^- (elliptic flow) [25,26] which has been observed at the Kaon Spectrometer (KaoS) [27,28].

This paper intends to give a comprehensive overview of the cross sections and emission patterns of the K^+ and K^- production in mass-symmetric heavy-ion reactions in the incident energy range from 0.6*A* to 2*A* GeV. It summarizes new as well as previously published [7,10,19,20,29] results on inclusive cross sections of Au+Au, Ni+Ni, and C+C collisions. Furthermore, new results are presented that focus on the centrality dependence of Ni+Ni collisions at 1.5*A* and at 1.93*A* GeV and of Au+Au collisions at 1.5*A* GeV. Results on the kaon production in the mass-asymmetric collision systems C+Au and Au+C have been published recently [30]. The results on the azimuthal distributions of kaons [27,28] as well as of pions and protons [31] have been published, and further publications on this topic are in preparation as is a review on pion production.

This paper is structured in the following way: First, in Sec. II, we describe the experimental setup and data analysis. In Sec. III A, we summarize the results on cross sections, energy distributions, and polar angle distributions for inclusive collisions, i.e., without any selection in the collision centrality. Section III B presents a detailed study of the centrality dependence of K^+ and K^- production. In Sec. IV A, the measured yields of K^+ and K^- mesons are discussed showing that their production is correlated. Despite this correlation of the production yields, the emission patterns of K^+ and K^- mesons differ significantly. Section IV B discusses these differences with respect to the influences of the *KN* potentials and with respect to different emission times of the two kaon species. Section IV C compares the production yields of K^+ mesons in different collision systems to recent transport-model calculations to extract information on the stiffness of the nuclear equation of state.

II. THE EXPERIMENT

A. The setup

The experiments were performed with the Kaon Spectrometer (KaoS) at the heavy-ion accelerator SIS (Schwerionensynchrotron) at the GSI (Gesellschaft für Schwerionenforschung) in Darmstadt, Germany. A detailed description is presented in Ref. [32]. Here we just briefly review the main features.

The setup of the quadrupole-dipole spectrometer KaoS is shown in Fig. 1. Positively and negatively charged particles are measured separately using different magnetic field polarities. The magnetic spectrometer has an acceptance in solid angle of $\Omega \approx 30$ msr and covers a momentum bite of $p_{\max}/p_{\min} \approx 2$. The short distance of 5–6.5 m from the target to the focal plane minimizes the number of kaon decays in flight. The loss of kaons by decay and due to the geometrical acceptance is accounted for by corrections which are determined by Monte Carlo simulations using the code GEANT [33]. Particle identification is based on momentum and time-of-flight (TOF) measurements. The trigger system is as well based on the time-of-flight information to separate pions, kaons, and protons. For the separation of high-momentum protons from kaons, a threshold Cherenkov detector [34] is used in addition. The trigger system suppresses pions and protons by factors of 10^2 and 10^3, respectively.

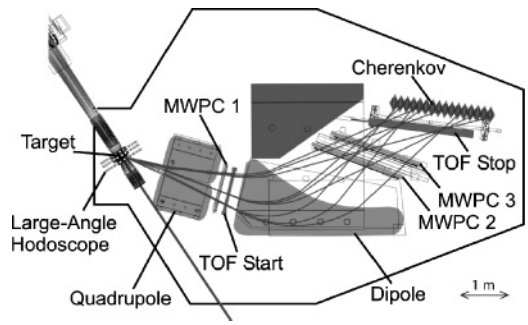

FIG. 1. Top view of the Kaon Spectrometer (KaoS) with its various detector components.

In total, there are three time measurements using segmented plastic scintillator arrays: The TOF start detector between the quadrupole and the dipole (16 modules), the TOF stop detector in the focal plane of the spectrometer (30 modules), and the large-angle hodoscope (LAH) around the target point covering polar laboratory angles of $12^\circ \leqslant \theta_{\rm lab} \leqslant 48^\circ$ (84 modules). The latter allows for a second time-of-flight measurement for background rejection and for the determination of the collision centrality using the number of measured charged particles.

The trajectory reconstruction is based on three large-area multiwire proportional counters (MWPC 1–3) [35], one between the quadrupole and the dipole and two behind the dipole magnet, each of them measuring two spatial coordinates. The efficiencies for kaon detection are greater than 95% for each of these detectors.

The beam intensity is monitored using two scintillator telescopes positioned at backward angles ($\theta_{\rm lab} = \pm 110^\circ$), measuring the flux of charged particles produced in the target which is proportional to the beam intensity. The absolute normalization is obtained in separate measurements at low beam intensities using a plastic scintillation detector directly in the beam line. The beam intensities are chosen such that the efficiency of the data acquisition system (DAQ) due to dead time is always above 50%.

The spectrometer is mounted on a platform which can be rotated around the target point on an air cushion in a polar angle range from $\theta_{\rm lab} = 0^\circ$ to 130°. The angular range covered at each position is $\Delta\theta_{\rm lab} = \pm 4^\circ$. Throughout this paper, we will always quote the mean value. The momentum coverage is maximized by measuring different magnetic field settings

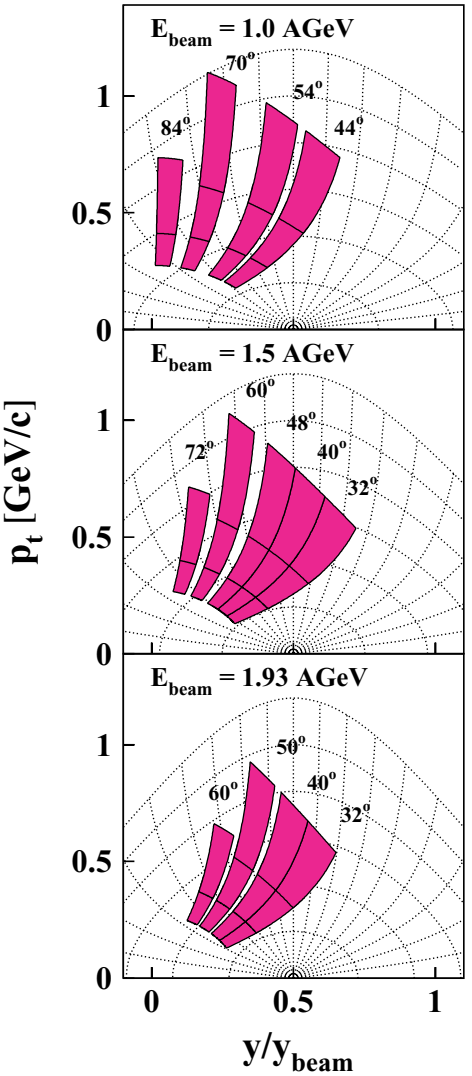

FIG. 2. (Color online) Examples of the coverage of the Kaon Spectrometer in transverse momentum p_t and in normalized rapidity $y/y_{\rm beam}$ for several laboratory angles $\theta_{\rm lab}$, various magnetic field settings, and three incident energies (as indicated).

($|B_{\rm dipole}| = 0.6, 0.9$, and 1.4 T). The resulting coverage for kaons in rapidity normalized to the beam rapidity $y/y_{\rm beam}$ and in transverse momentum p_t is sketched in Fig. 2 for three different beam energies ($1.0A$, $1.5A$, and $1.93A$ GeV). The shaded areas correspond to different angular settings $\theta_{\rm lab}$ of the spectrometer in the laboratory as denoted in the figure and to various magnetic field settings.

In this paper we report on measurements of the collision systems C+C ($0.8A$, $1.0A$, $1.2A$, $1.5A$, $1.8A$, and $2.0A$ GeV beam energy), Ni+Ni ($1.1A$, $1.5A$, and $1.93A$ GeV), and Au+Au ($0.6A$, $0.8A$, $1.0A$, $1.135A$, and $1.5A$ GeV). The targets as well as their respective thicknesses and interaction probabilities are given in Table I. Because of the energy loss in the Au targets, the average effective beam energies $E_{\rm beam}^{\rm eff}$ for kaon production in these cases are $0.56A$, $0.78A$, $0.96A$, $1.1A$, and $1.48A$ GeV. For the other target materials, the energy loss is negligible. Throughout the text we use the values of the nominal beam energies $E_{\rm beam}$.

TABLE I. Thicknesses and interaction probabilities for targets used in the various experiments.

Target	Thickness (mm)	Interact. prob.
C	3.0	2.7%
Ni	0.8	2.1%
Au ($0.6A$, $1.0A$, $1.135A$ GeV)	1.0	3.6%
Au ($0.8A$, $1.5A$ GeV)	0.5	1.8%

However, in all figures displaying data as a function of the beam energy, the data points are plotted at $E_{\rm beam}^{\rm eff}$.

In the case of the $1.5A$ GeV Au beam, an exceptional operation of the GSI accelerator facility was required: acceleration of $^{197}Au^{63+}$ ions with the synchrotron SIS up to an energy of $0.3A$ GeV, then extraction and full stripping, followed by injection into the experimental storage ring (ESR) where the beam was cooled (electron cooling), and finally reinjection into the SIS and acceleration up to $1.5A$ GeV.

B. Data analysis

1. Track reconstruction

For the reconstruction of particle tracks in the spectrometer, reconstruction functions correlating the spatial coordinates measured by different detectors are used to combine the information of different detectors to track candidates. For example, one reconstruction function is used to calculate the x coordinate in the MWPC between the quadrupole and the dipole (x_1) as a function of the x coordinates of the two MWPCs behind the dipole (x_2, x_3). By comparing a measured position in one detector with the calculated position based on the hits in other detectors using the reconstruction functions, track candidates are created. This is done for the spatial coordinates in the MWPCs as well as for the assignment of the modules of the TOF detectors.

The reconstruction functions are determined by Monte Carlo simulations using a complete description of the experimental setup within GEANT. Single tracks are followed through the spectrometer, and the correlation functions are determined by fitting polynomial functions up to seventh order and with up to three x coordinates and up to three y coordinates to all these simulated tracks.

After the reconstruction, a resulting track candidate consists of x and y coordinates in all three MWPCs, the module numbers, the time and energy-loss information of the TOF start and stop detectors as well as the time and multiplicity information of the LAH.

To determine the efficiency of the tracking procedure, GEANT is used. This time not only single tracks are generated but also combinations of one or several tracks and additional background hits in the different detectors as observed in the experiment. The resulting efficiencies vary with the laboratory angle, the magnetic field strength, and the size of the collision system because of varying track and background multiplicities. The resulting efficiencies of the tracking procedure are always over 90%.

For each track candidate constructed in the preceding steps, the momentum $p_{\rm lab}$ and the length of the flight path Δl between

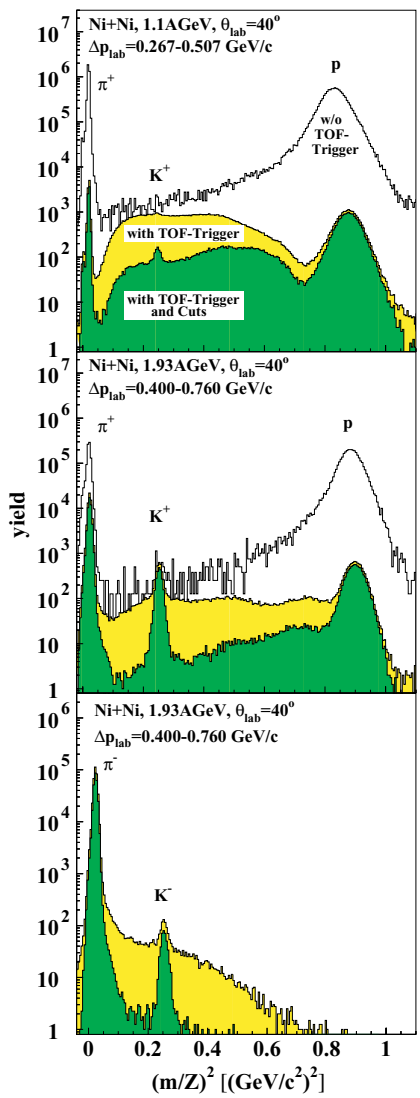

FIG. 3. (Color online) Distributions of the squares of the masses assigned to the reconstructed tracks in three different cases: Ni+Ni collisions at 1.1A GeV (upper panel), at 1.93A GeV (middle panel), both using the field polarity for positively charged particles, and at 1.93A GeV for negatively charged particles (lower panel). Differently shaded areas show the impact of the TOF trigger and of the application of the selection criteria during the data analysis.

the TOF start and stop detector modules are obtained from a lookup table generated with GEANT. From these quantities, together with the measured time difference Δt between the two TOF detectors, the squared mass over charge ratio $(m/Z)^2$ is calculated using

$$\left(\frac{m}{Z}\right)^2 = \left(\frac{p_{\rm lab}\cdot c}{Z}\right)^2 \left[\left(\frac{\Delta t\cdot c}{\Delta l}\right)^2 - 1\right]. \qquad (1)$$

Since the particles under investigation have $Z = 1$, we simply use mass in the following.

2. *Background reduction and cross section calculation*

Figure 3 shows mass distributions for Ni+Ni collisions at $\theta_{\rm lab} = 40^\circ$. The distribution in the upper panel has been measured at a beam energy of 1.1A GeV and at particle momenta $p_{\rm lab} = 0.267$–0.507 GeV/c using the magnetic field setting for positively charged particles. In this case of low beam energy and low particle momenta, the region of the kaon mass is dominated by background. The distribution labeled "w/o TOF-Trigger" was measured using trigger conditions that forced every particle passing through the spectrometer to be recorded. The distribution labeled "with TOF-Trigger" shows the clear reduction of pions and protons being recorded when using the time-of-flight trigger, but still no clear K^+ signal can be seen. The situation is different at higher beam energies or at higher particle momenta, where the kaons are clearly visible already in the distributions "with TOF-Trigger" as can be seen in the two lower panels of Fig. 3. They show mass distributions for Ni+Ni at 1.93A GeV for positively charged particles in the middle panel and for negatively charged particles in the lower panel. In the latter case, the trigger condition "w/o TOF-Trigger" was not measured.

To reduce the remaining background effectively without losing too many kaons, two types of selection criteria are applied:

(i) The so-called geometrical cuts: These selection criteria are based on the comparison between measured positions in one of the MWPCs and those extrapolated from hits in the other two using the reconstruction functions described in the previous section. These selection criteria are adjusted using measurements during the same experiment which are nearly free of background (highest beam energy and/or largest laboratory angle). This can be done because the particle trajectories inside the spectrometer depend only on the magnetic field and geometrical setup but not on quantities such as $\theta_{\rm lab}$ or $E_{\rm beam}$.

(ii) The so-called velocity cut: For each track candidate, the particle velocity between the TOF start detector and the TOF stop detector is calculated as well as the velocity between the large-angle hodoscope and the TOF stop detector. The comparison of these two velocities is a powerful tool for suppressing background created by fake track candidates. The velocity cut is adjusted by using the measurements nearly free of background as in the case of the geometrical cuts.

Depending on the initial signal-to-background ratio, the strength of these cuts is varied between 5σ and 2σ. After the application of the selection criteria, the final signal-to-background ratio varies between 0.7 and 120. The impact of the cuts on the mass distributions is as well shown in Fig. 3 (labeled "with TOF Trigger and Cuts"). In many cases, the remaining background is rather small, as can be clearly seen in the two lower mass distributions measured at 1.93A GeV. Even in the case of low beam energy and low particle momenta, a clear K^+ signal can be observed after applying the selection criteria (upper panel, please note the logarithmic scale).

To subtract the remaining background in the mass distributions, a combined fit using a Gaussian and a polynomial function to the mass distribution is performed within a window around the kaon mass. The polynomial part is used to estimate the background below the kaon peak and is subtracted. Figure 4 shows mass distributions for Ni+Ni collisions at

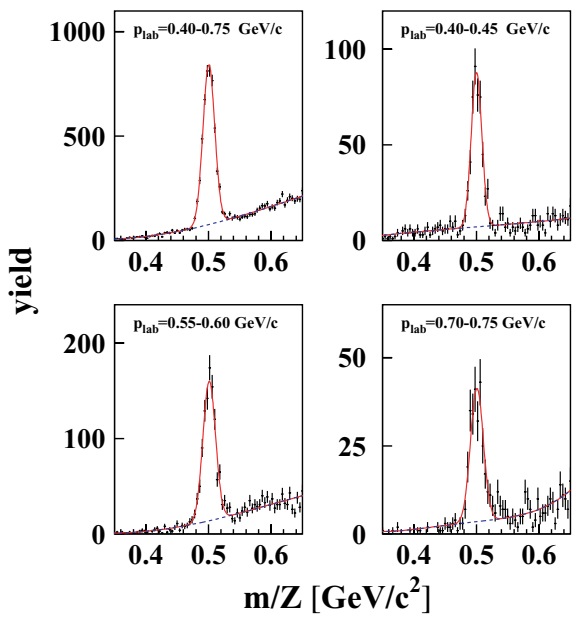

FIG. 4. (Color online) Mass distributions for Ni+Ni collisions at $1.1A$ GeV at $\theta_{\rm lab} = 40^\circ$ for different particle momenta as indicated. Solid lines depict results of a combined fit to the background and to the peak at the kaon mass; dashed lines show only the background part.

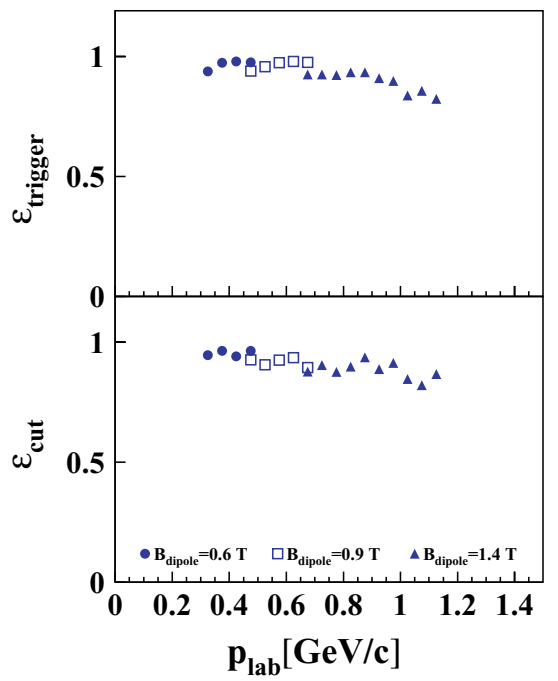

FIG. 5. (Color online) Trigger efficiencies $\epsilon_{\rm trigger}(p_{\rm lab})$ for Ni+Ni at $1.1A$ GeV for the three magnetic field settings measured (upper panel), and efficiencies of the applied selection criteria $\epsilon_{\rm cut}(p_{\rm lab})$ (lower panel) for the same data set.

$1.1A$ GeV at $\theta_{\rm lab} = 40^\circ$ as an example with a significant background contamination. The fits are performed separately for each bin in particle momentum (in most cases having a width of 0.05 GeV/c); the upper left graph shows the distribution integrated over the full momentum range of this particular magnetic field setting for illustration purposes only. The solid lines depict the result of the combined fit to the background and to the peak at the kaon mass, the dashed lines show the background part only.

The cross sections are calculated from the number of kaons $N(p_{\rm lab}\,,\Omega_{\rm lab})$ as

$$\frac{d^2\sigma}{dp_{\rm lab}d\Omega_{\rm lab}} = N(p_{\rm lab}\,,\Omega_{\rm lab})\frac{M_{\rm target}}{\rho_{\rm target}d_{\rm target}N_A} \times \frac{1}{N_{\rm proj}}\frac{1}{f_{\rm acc}(p_{\rm lab}\,,\Omega_{\rm lab})}\frac{1}{\epsilon(p_{\rm lab})} \qquad (2)$$

with $M_{\rm target}$ being the molar mass, $\rho_{\rm target}$ the density, and $d_{\rm target}$ the thickness of the target material. N_A denotes Avogadro's constant, and $N_{\rm proj}$ the number of projectiles impinging on the target.

The correction for the geometrical acceptance of the spectrometer and for the particle decay $f_{\rm acc}(p_{\rm lab}, \Omega_{\rm lab})$ is calculated using a GEANT simulation. The simulated data sets are analyzed with the same analysis procedure as the experimental data. The correction is deduced from the ratio of particles found after the analysis to those initially simulated.

The total efficiency $\epsilon(p_{\rm lab})$ is calculated by multiplying the detector, the DAQ, and the tracking efficiencies described before as well as the trigger efficiency $\epsilon_{\rm trigger}(p_{\rm lab})$ and the efficiency of the application of the selection criteria $\epsilon_{\rm cut}(p_{\rm lab})$.

To determine the efficiency of the trigger system (which is based on particle velocities) pions and protons measured at magnetic fields scaled by the mass ratios $m_{\rm pion}/m_{\rm kaon}$ or $m_{\rm proton}/m_{\rm kaon}$ are used, which then have the same velocities as kaons measured at the nominal fields. These pions and protons are called "TOF-simulated kaons" in the following. Using an open trigger condition that forces every event for which a particle enters the spectrometer to be recorded (w/o TOF) and keeping track of the decisions the TOF trigger would have taken, the efficiency of the TOF trigger can be determined. The resulting trigger efficiencies are over 90% but they depend on the particle momentum. The upper panel of Fig. 5 shows $\epsilon_{\rm trigger}(p_{\rm lab})$ for Ni+Ni at $1.1A$ GeV for the three magnetic field settings measured ($|B_{\rm dipole}| = 0.6$, 0.9, and 1.4 T).

The efficiency of the applied selection criteria as a function of $p_{\rm lab}$ is determined using the background-free measurements as described above. In some data sets, the statistics of these settings were not sufficient. In these cases, the efficiencies of the geometrical cuts were determined using GEANT simulations, and the efficiency of the velocity cut was determined using the TOF-simulated kaons. This method has been validated by comparing its results to efficiencies calculated from real data in cases where this is possible. The resulting efficiencies range from 75% to 100%. For the example Ni+Ni at $1.1A$ GeV, they are depicted in the lower panel of Fig. 5.

Figure 6 shows the resulting differential cross sections for K^+ mesons in Ni+Ni collisions at $1.1A$ GeV at $\theta_{\rm lab} = 40^\circ$ according to Eq. (2) as a function of $p_{\rm lab}$. This momentum distribution consists of data measured at three different magnetic field settings ($|B_{\rm dipole}| = 0.6$, 0.9, and 1.4 T) which are analyzed separately but overlap very well.

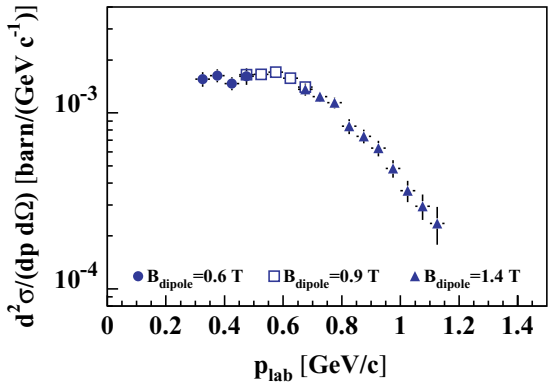

FIG. 6. (Color online) Differential cross section as a function of $p_{\rm lab}$ for K^+ in Ni+Ni collisions at 1.1A GeV at $\theta_{\rm lab} = 40^\circ$. The different symbols denote data measured at different magnetic field settings.

III. EXPERIMENTAL RESULTS

A. Inclusive reactions

In this section, the inclusive cross sections for the production of K^+ and of K^- mesons in C+C, Ni+Ni, and Au+Au collisions are presented as a function of their laboratory momentum $p_{\rm lab}$ as well as their energy $E_{\rm c.m.}$ and their emission angle $\theta_{\rm c.m.}$ in the center-of-momentum frame. Inclusive means that no centrality selection was applied to the data, neither in the analysis nor implicitly by the experimental setup or the trigger. Let us recall that the trigger is generated by a time-of-flight signal in the spectrometer and that the multiplicity detector is not part of the trigger system. The determination of the functional dependencies of the production cross sections on $E_{\rm c.m.}$ and $\theta_{\rm c.m.}$ allows for an extrapolation to phase space areas not covered by the experiment and for a determination of integrated production yields. All results of this section are summarized in Table II. Throughout the figures of this paper we use a consistent color code for an easy distinction of the collision systems while of course keeping full descriptions for black-and-white printed versions: Results of Au+Au collisions appear in red, Ni+Ni in blue, and C+C in green.

Some of the data sets presented in this section are published here for the first time, others have already been published [7,19,20,29]. As slightly different procedures were used in those publications to extrapolate and integrate the data, we have recalculated the total production cross sections using one consistent procedure for all data sets. Earlier measurements with large errors are not taken into account [36–38].

TABLE II. Summary of the integrated production cross sections of K^+ and of K^- mesons. Inverse slope parameters $T_{\rm sf}$ and $T_{\rm midrap}$ and angular anisotropies $a_2^{\rm sf}$ and $a_2^{\rm div}$ were determined by two different procedures as explained in the text. For systems with only one measured angle $\theta_{\rm lab}$, the angular anisotropies $a_2^{\rm sf}$ were not fitted but set to an interval guided by neighboring beam energies. It is given in square brackets. Additional errors for σ and $T_{\rm sim}$ due to this procedure are denoted by the superscript "a_2".

Reaction	$E_{\rm beam}$ [A GeV]	$\theta_{\rm lab}$ [deg]	σ [mb]	$T_{\rm sf}$ [MeV]	$a_2^{\rm sf}$	$T_{\rm midrap}$ [MeV]	$a_2^{\rm div}$
K^+							
C+C	0.8	44	$0.016 \pm 0.002^{\rm stat} \pm 0.0016^{\rm syst} \pm 0.002^{a_2}$	$54 \pm 4 \pm 1^{a_2}$	[−0.5, 0.5]	52 ± 4	–
	1.0	44,54,70	$0.1 \pm 0.01^{\rm stat} \pm 0.01^{\rm syst}$	60 ± 3	0.25 ± 0.27	56 ± 4	0.18 ± 0.27
	1.2	40	$0.3 \pm 0.03^{\rm stat} \pm 0.03^{\rm syst} \pm 0.02^{a_2}$	$67 \pm 4 \pm 2^{a_2}$	[0.0, 1.0]	67 ± 5	–
	1.5	32,48	$1.3 \pm 0.1^{\rm stat} \pm 0.13^{\rm syst}$	77 ± 3	0.67 ± 0.30	77 ± 5	0.71 ± 0.23
	1.8	32,40,48,60	$3.15 \pm 0.13^{\rm stat} \pm 0.32^{\rm syst}$	81 ± 2	1.21 ± 0.15	81 ± 3	1.25 ± 0.14
	2.0	32,40	$5.1 \pm 0.3^{\rm stat} \pm 0.5^{\rm syst}$	86 ± 3	1.13 ± 0.23	85 ± 5	1.12 ± 0.17
Ni+Ni	1.1	40	$5.9 \pm 0.3^{\rm stat} \pm 0.6^{\rm syst} \pm 0.3^{a_2}$	$87 \pm 3 \pm 1^{a_2}$	[0.5, 1.0]	87 ± 4	–
	1.5	40	$31.4 \pm 1.3^{\rm stat} \pm 3.1^{\rm syst} \pm 1.7^{a_2}$	$101 \pm 3 \pm 3^{a_2}$	[0.5, 1.0]	97 ± 7	–
	1.93	32,40,50,60	$95 \pm 2^{\rm stat} \pm 9.5^{\rm syst}$	112 ± 2	0.90 ± 0.06	108 ± 5	0.85 ± 0.06
Au+Au	0.6	50	$0.5 \pm 0.1^{\rm stat} \pm 0.05^{\rm syst} \pm 0.03^{a_2}$	$49 \pm 6 \pm 1^{a_2}$	[0.75, 1.25]	50 ± 7	–
	0.8	44,84	$8.7 \pm 1.4^{\rm stat} \pm 0.9^{\rm syst}$	67 ± 4	1.20 ± 0.42	66 ± 5	1.25 ± 0.4
	1.0	44,84	$31.4 \pm 4^{\rm stat} \pm 3.1^{\rm syst}$	82 ± 3	1.07 ± 0.24	81 ± 6	1.16 ± 0.2
	1.135	56	$65 \pm 14^{\rm stat} \pm 6.5^{\rm syst} \pm 2^{a_2}$	$89 \pm 9 \pm 1^{a_2}$	[0.75, 1.25]	–	–
	1.5	32,40,48,60,72	$346 \pm 9^{\rm stat} \pm 35^{\rm syst}$	111 ± 2	1.25 ± 0.09	111 ± 5	1.28 ± 0.09
K^-							
C+C	1.5	40	$0.016 \pm 0.006^{\rm stat} \pm 0.0016^{\rm syst} \pm 0.001^{a_2}$	$50 \pm 12 \pm 7^{a_2}$	[0.0, 1.0]	–	–
	1.8	40,60	$0.078 \pm 0.01^{\rm stat} \pm 0.008^{\rm syst}$	65 ± 8	0.80 ± 0.25	55 ± 8	–
	2.0	40	$0.15 \pm 0.03^{\rm stat} \pm 0.015^{\rm syst} \pm 0.004^{a_2}$	$57 \pm 7 \pm 2^{a_2}$	[0.5, 1.5]	58 ± 9	–
Ni+Ni	1.5	40	$0.58 \pm 0.05^{\rm stat} \pm 0.06^{\rm syst} \pm 0.03^{a_2}$	$89 \pm 6 \pm 2^{a_2}$	[0.5, 1.0]	98 ± 10	–
	1.93	32,40,50,60	$2.6 \pm 0.1^{\rm stat} \pm 0.26^{\rm syst}$	89 ± 2	0.70 ± 0.09	84 ± 4	0.66 ± 0.09
Au+Au	1.5	32,40,48,60	$5.0 \pm 0.4^{\rm stat} \pm 0.5^{\rm syst}$	87 ± 4	0.56 ± 0.26	91 ± 8	0.64 ± 0.26

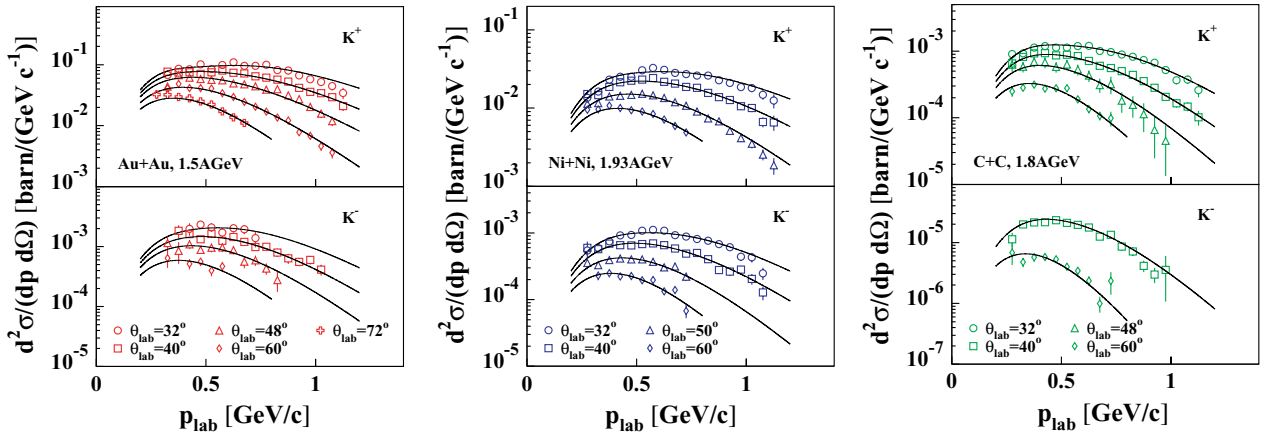

FIG. 7. (Color online) Inclusive production cross sections for K^+ and for K^- as a function of the laboratory momentum $p_{\rm lab}$ for inclusive reactions of Au+Au at 1.5A GeV, Ni+Ni at 1.93A GeV, and C+C at 1.8A GeV. The lines represent a simultaneous fit to all laboratory angles using the distribution according to Eq. (5).

1. Energy distributions

Figure 7 shows the inclusive production cross sections for K^+ (upper panels) and for K^- (lower panels) as a function of their momentum $p_{\rm lab}$ in the laboratory system for three different collision systems. The figure depicts data taken in Au+Au collisions at a beam energy of 1.5A GeV, in Ni+Ni at 1.93A GeV, and in C+C at 1.8A GeV. To obtain a wide coverage of the phase space (see Fig. 2) measurements at several polar angle settings of the spectrometer in the laboratory $\theta_{\rm lab}$ were performed. The lines in Fig. 7 are the results of simultaneous fits to all angular settings measured for a given system assuming a Maxwell-Boltzmann shaped dependence of the invariant production cross section on the center-of-momentum energy $E_{\rm c.m.}$ and a quadratic dependence on the cosine of the polar emission angle in the c.m. system $\theta_{\rm c.m.}$. This procedure will be discussed in detail later.

The necessity for using a nonisotropic distribution in $\theta_{\rm c.m.}$ is depicted in Fig. 8. Here the invariant cross sections $\sigma_{\rm inv} = E\frac{d^3\sigma}{dp^3}$ are shown as a function of the kinetic energy in the c.m. system $E_{\rm c.m.} - m_0c^2$ for Au+Au at 1.5A GeV. Full symbols denote K^+, open symbols K^-. The data measured at a small angle in the laboratory system (K^+: $\theta_{\rm lab} = 32°$, K^-: $\theta_{\rm lab} = 40°$) are depicted by circles, those measured at a large angle (K^+: $\theta_{\rm lab} = 72°$, K^-: $\theta_{\rm lab} = 60°$) are represented by squares. The lines are Maxwell-Boltzmann distributions

$$E\frac{d^3\sigma}{dp^3} \sim E_{\rm c.m.} \exp\left(-\frac{E_{\rm c.m.}}{T}\right) \tag{3}$$

fitted to the data, with T being the inverse slope parameter. For an isotropic emission in the c.m. system, all spectra of a given particle type are expected to fall on top of each other regardless of the laboratory angle at which they have been measured. For K^+ mesons, this is clearly not the case, pointing toward an anisotropic emission.

Since the distributions have been measured at fixed values of $\theta_{\rm lab}$ in the laboratory, data points at different particle energies correspond to different emission angles $\theta_{\rm c.m.}$ in the c.m. system. Therefore, this anisotropy might affect the determination of the inverse slope parameter T of the energy spectra if data measured at a fixed $\theta_{\rm lab}$ would be transformed into the c.m. system and then fitted.

Therefore, we created "midrapidity distributions" by selecting data points within $\theta_{\rm c.m.} = 90° \pm 10°$ from measurements at various laboratory angles. The results are shown in Fig. 9, which summarizes the energy distributions of the K^+ and K^- production as measured in three different collision systems (Au+Au, Ni+Ni, C+C) at different incident energies (0.6A up to 2A GeV). The measurements of K^+ in Au+Au at 1.135A GeV and of K^- in C+C at 1.5A GeV are not displayed

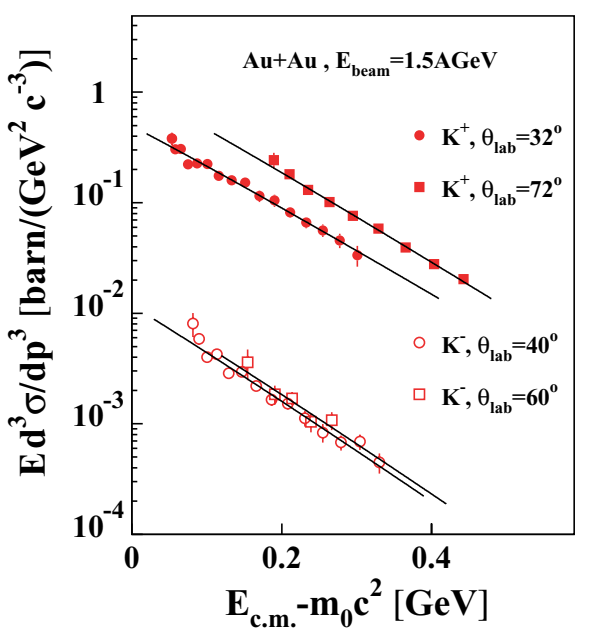

FIG. 8. (Color online) Invariant cross sections for K^+ (full symbols) and for K^- (open symbols) in inclusive Au+Au collisions at 1.5A GeV, both at different laboratory angles. The lines represent fits according to Eq. (3). The observation that the data measured at different laboratory angles do not coincide indicates a nonisotropic polar angle distribution.

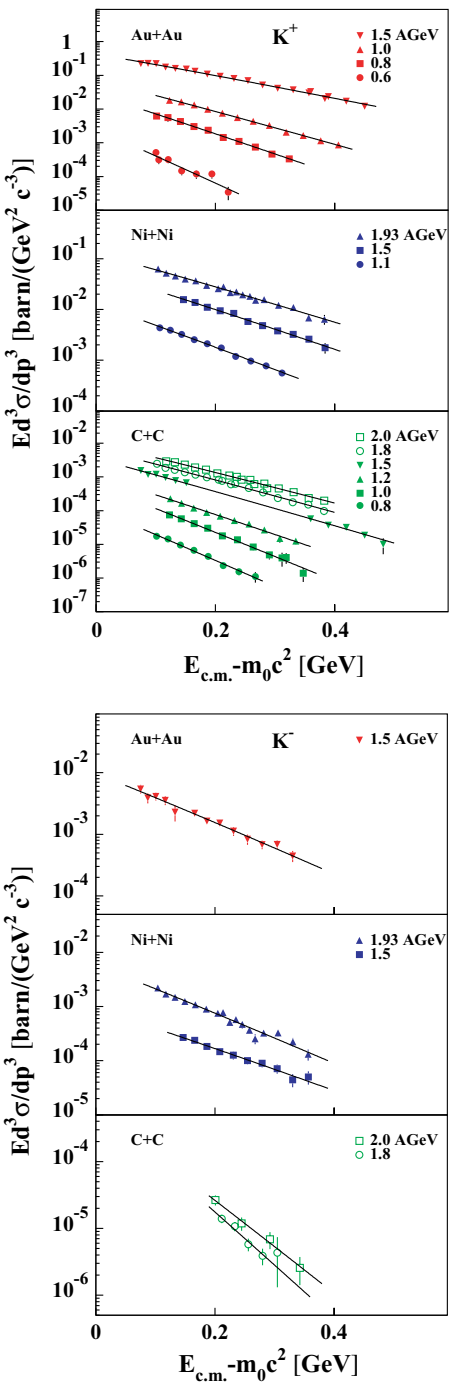

FIG. 9. (Color online) Inclusive invariant cross sections at midrapidity as a function of the kinetic energy $E_{\mathrm{c.m.}} - m_0c^2$ for K^+ and K^- for the various collision systems and beam energies measured. The midrapidity condition is a selection of $\theta_{\mathrm{c.m.}} = 90^\circ \pm 10^\circ$.

in Fig. 9 because they do not cover midrapidity. The lines are fits to the data according to Eq. (3). The resulting inverse slope parameters T_{midrap} are given in Table II.

2. *Polar angle distributions*

To extract the angular emission pattern, we assume that the dependence of the invariant cross sections on the polar angle $\theta_{\mathrm{c.m.}}$ and on the energy $E_{\mathrm{c.m.}}$ can be factorized. The energy dependence is determined at midrapidity by fitting Maxwell-Boltzmann distributions to the data as described above and shown in Fig. 9. As already mentioned, each of the data points measured at a given center-of-momentum energy $E_{\mathrm{c.m.}}$ and a laboratory angle θ_{lab} corresponds to a different emission angle $\theta_{\mathrm{c.m.}}$ in the center-of-momentum frame.

To disentangle the dependencies on the energy and on the polar emission angle, we normalized each measured data point $\sigma_{\mathrm{inv}}(E_{\mathrm{c.m.}}, \theta_{\mathrm{c.m.}})$ to the corresponding value $\sigma_{\mathrm{inv}}(E_{\mathrm{c.m.}}, \theta_{\mathrm{c.m.}} = 90^\circ)$. The latter is determined using the fits to "midrapidity distributions" according to Eq. (3). Assuming that the energy dependence of the kaon production is fully described by these midrapidity fits, the results are the polar angle emission patterns. They are shown in Fig. 10 as a function of $\cos(\theta_{\mathrm{c.m.}})$ for Au+Au at 1.5A GeV and for Ni+Ni at 1.93A GeV. Full symbols are measured data points; open symbols have been reflected at $\theta_{\mathrm{c.m.}} = 90^\circ$ since for mass-symmetric systems the polar angle distributions have to be symmetric around $\theta_{\mathrm{c.m.}} = 90^\circ$. Both systems show a forward-backward preference in the emission pattern which is more pronounced for K^+ than for K^-.

To quantify the anisotropy, the distributions have been fitted with a quadratic dependence on $\cos(\theta_{\mathrm{c.m.}})$

$$\frac{d\sigma}{d\cos(\theta_{\mathrm{c.m.}})} \sim 1 + a_2^{\mathrm{div}} \cos^2(\theta_{\mathrm{c.m.}}) \tag{4}$$

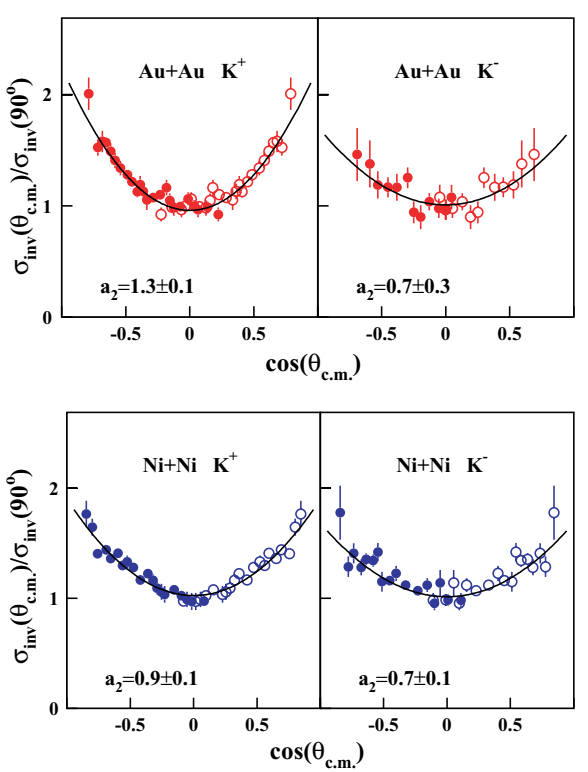

FIG. 10. (Color online) Polar angle distributions for inclusive Au+Au collisions at 1.5A GeV and Ni+Ni at 1.93A GeV. Full symbols denote measured data, open symbols are reflected at $\theta_{\mathrm{c.m.}} = 90^\circ$. The lines represent fits according to Eq. (4).

as depicted by the lines in the figure. This procedure has been applied to most data sets, resulting in the values for $a_2^{\rm div}$ as given in Table II. In the cases for which only one laboratory angle has been measured, the coverage in $\theta_{\rm c.m.}$ is rather small, making the determination of $a_2^{\rm div}$ impossible.

The super(sub)scripts "div" for the angular anisotropy and "midrap" for the inverse slope parameters are used for the two-step procedure presented above. Since the energy dependence of the kaon production is well described by a Maxwell-Boltzmann distribution and the polar angle distribution by a quadratic dependence on $\cos(\theta_{\rm c.m.})$, we additionally performed simultaneous fits to all momentum distributions measured at different laboratory angles $\theta_{\rm lab}$ for a given system, using the combined function

$$E\frac{d^3\sigma}{dp^3} = C\left[1 + a_2^{\rm sf}\cos^2(\theta_{\rm c.m.})\right] E_{\rm c.m.}\exp\left(-\frac{E_{\rm c.m.}}{T_{\rm sf}}\right), \quad (5)$$

with $a_2^{\rm sf}$, $T_{\rm sf}$, and the normalization C being the three variable parameters. The results of this procedure are denoted by "sf". For Au+Au at 1.5A GeV, Ni+Ni at 1.93A GeV, and C+C at 1.8A GeV, the results of these fits are shown as solid lines in Fig. 7. The parameters obtained for all collision systems at all beam energies are given in Table II. They agree very well with the values obtained by the two-step procedure denoted by $T_{\rm midrap}$ and by $a_2^{\rm div}$. The combined fits also provide the correlations between the three parameters and thus the full error matrix which is necessary for calculating the errors of the integrated production cross sections. In those cases for which only one angle has been measured, we take an interval for the polar angle anisotropy $a_2^{\rm sf}$, denoted by square brackets in Table II, with values set according to the trend at neighboring beam energies. This variation of $a_2^{\rm sf}$ yields additional errors on the inverse slope parameters $T_{\rm sf}$ as well as on the integrated cross sections as tagged by the superscript "a_2" in Table II.

3. *Total production cross sections*

The results of the simultaneous fits have been used to extrapolate the data to phase-space regions not covered by the experiment and to calculate total production cross sections by integrating Eq. (5) over the full phase space. The extrapolation in $E_{\rm c.m.}$ contributes about 35% to the total production cross sections. The resulting total production cross sections for K^+ and K^- for all collision systems and for all beam energies are summarized in Table II. The error bars of the data points in the figures showing energy spectra and polar angle distributions contain the statistical uncertainties as well as point-to-point systematic errors due to the background subtraction. The overall systematic error of the absolute normalization is stated separately in Table II and is quadratically added to the statistical errors in all figures comparing cross sections or multiplicities from different collision systems.

In several cases, only one polar angle has been measured. As already described for the inverse slope parameters T in the previous section, for each of those cases, an interval for a_2 guided by the systematics given by neighboring beam energies has been used to determine an additional error on the integrated cross section σ denoted by the superscript "a_2" in Table II.

Part of the data has been published earlier, with the methods used to extrapolate the measured data to the full phase space being slightly different in the various publications. In this paper, we consistently apply one single method to extrapolate and integrate the data.

For C+C collisions, σ and T for K^+ and for K^- were published [19] assuming the angular anisotropy contributes 20% to the total cross section independent of the incident energy, which is equivalent to $a_2 = 0.6$. Now we determine a_2 for each measurement separately. The differences between the values for σ and T in Table II and those published in [19] are nevertheless smaller than the statistical errors.

In the case of Ni+Ni, cross sections for the K^+ and the K^- production at 1.93A GeV have been published in [20] with the angular anisotropy being taken from a two-step procedure rather than from a simultaneous fit. Also in this case, the differences between the results in Table II and the previously published values are smaller than the statistical errors.

For Au+Au, the values for σ, T, and a_2 have been published for K^+ [7]. The results in Table II for 0.6A, 0.8A, 1.0A, and 1.135A GeV differ from the published values by less than the statistical errors. For K^+ at 1.5A GeV, the results published in Ref. [7] are $\sigma = 267 \pm 30$ mb, $T = 100 \pm 5$ MeV, and $a_2 = 1.06 \pm 0.3$. They correspond to a low statistics measurement using a thicker target, thus reducing the effective beam energy for the K^+ production to 1.46A GeV. This difference in effective energy accounts for a difference of about 10% in cross section compared with the new high statistics experiment reported on in this paper using a thinner target (with $E_{\rm eff} = 1.48A$ GeV). In addition in the experiment described in Ref. [7], the anisotropy in the polar angle emission pattern was underestimated because of a reduced coverage in $\theta_{\rm lab}$, which accounted for an additional 5% difference in the cross section.

To calculate particle multiplicities M, the integrated production cross sections σ (see Table II) need to be divided by the total reaction cross section σ_r which cannot be determined easily because the particle-multiplicity distribution measured with a multiplicity trigger condition has a cutoff at low multiplicities (see also Sec. III B). Therefore, we determined the reaction cross sections using Glauber calculations [39] resulting in σ_r(Au+Au) = 6.8 b, σ_r(Ni+Ni) = 3.1 b, and σ_r(C+C) = 0.95 b. Figure 11 summarizes the multiplicities of K^+ and of K^- mesons as a function of the beam energy as determined in inclusive reactions (Au+Au, Ni+Ni, C+C) and normalized to the mass number A of the respective colliding nuclei. Both particle species exhibit strongly rising excitation functions as expected due to the proximity of the thresholds in binary NN collisions (1.58 GeV for K^+, 2.5 GeV for K^-). The solid lines reflect fits according to the formula [40]

$$\frac{M_K}{A} = C\sqrt{T_{\rm max}}\exp\left[-\frac{E_{\rm thr}}{T_{\rm max}}\right], \quad (6)$$

with $T_{\rm max} = T_0(E_{\rm beam})^\eta$. The variable parameters in the fit are C, T_0, and η. For both K^+ and K^-, the multiplicities per mass number A increase with system size from C+C to Au+Au at the same incident energy.

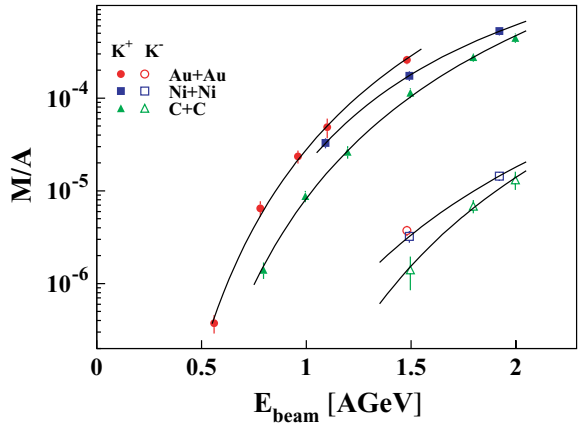

FIG. 11. (Color online) Multiplicities of K^+ (full symbols) and of K^- mesons (open symbols) per mass number A of the respective collision system as a function of the beam energy. The lines represent fits to the data according to Eq. (6).

B. Centrality dependence

The collision centrality was derived from the multiplicity of charged particles measured in the large-angle hodoscope ($Mult_{\mathrm{LAH}}$). Figure 12 shows the respective multiplicity distributions for Au+Au at 1.5A GeV and for Ni+Ni at 1.93A GeV measured with a multiplicity trigger. To study the centrality dependence of the K^+ and K^- production, the data were grouped into five centrality bins for Ni+Ni at both 1.5A and at 1.93A GeV as well as for Au+Au at 1.5 A GeV. These bins are also depicted in Fig. 12. The distributions have been normalized to the beam intensity, to the target thickness, and to the efficiency of the DAQ system so that the area between the respective bin boundaries represents the corresponding fraction of the total reaction cross sections σ_r for a given bin. Very peripheral collisions in the first centrality bin might be missed by the multiplicity trigger; however, kaons from such peripheral events are measured since they are triggered by the time-of-flight trigger in the spectrometer. The fraction of σ_r for this most peripheral bin is determined by taking the total reaction cross section from a Glauber calculation [39] and subtracting the sum of the experimentally measured values of the four other centrality bins. For Au+Au, the five bins correspond to 0–5.4%, 5.4–18.1%, 18.1–31.1%, 31.1–52.3%, and 52.3–100% of σ_r from central to peripheral collisions; for Ni+Ni, to 0–4.4%, 4.4–15.0%, 15.0–26.5%, 26.5–45.9%, and 45.9–100.0% of σ_r. The corresponding mean numbers of participating nucleons A_{part} have also been calculated using Glauber calculations.

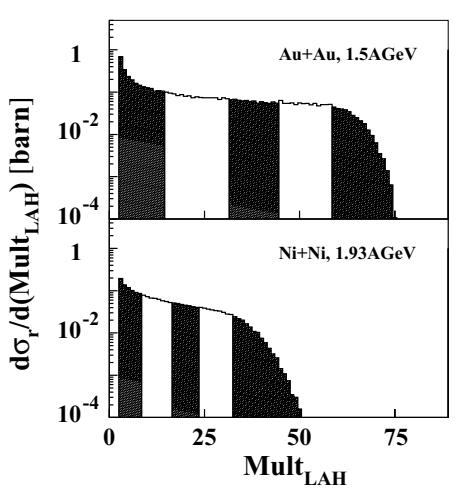

FIG. 12. Reaction cross section as a function of the charged particle multiplicity in the LAH for Au+Au collisions at 1.5A GeV and for Ni+Ni at 1.93A GeV. The shaded areas denote the five centrality bins.

1. Multiplicities

The multiplicity of a particle species for each centrality bin is defined as $M = \sigma/(f\sigma_r)$ with σ being the production cross section for the respective particle species and $(f\sigma_r)$ being the fraction of the total reaction cross section for the respective bin. Figure 13 presents the multiplicities per number of participating nucleons M/A_{part} as a function of A_{part} at a beam energy of 1.5A GeV for Au+Au and Ni+Ni. To calculate these multiplicities, only data measured at $\theta_{\mathrm{lab}} = 40^\circ$ were used, because for Ni+Ni this is the only laboratory angle measured at that beam energy. The K^+ are shown in the upper panel, the K^- in the middle panel, and the pions in the lower panel. Since neutral particles cannot be detected by the spectrometer, the total pion multiplicity was calculated as $M(\pi) = 3/2M(\pi^+) + 3/2M(\pi^-)$.

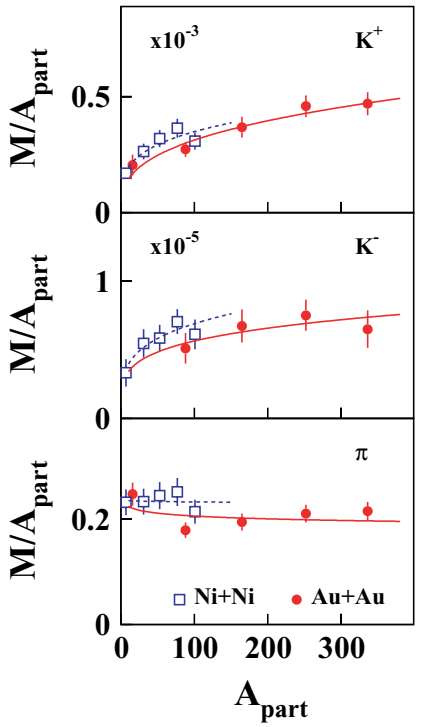

FIG. 13. (Color online) Dependence of multiplicities of K^+ and K^- mesons as well as of pions on A_{part}. Full symbols denote Au+Au, open symbols Ni+Ni, both at 1.5A GeV. The lines are functions $M \sim A_{\mathrm{part}}^{\alpha}$ fitted to the data separately for Au+Au (solid lines) and Ni+Ni (dashed lines). The data have been measured at $\theta_{\mathrm{lab}} = 40^\circ$.

The lines in Fig. 13 are functions $M \sim A_{\rm part}^{\alpha}$ fitted to the data separately for Au+Au and for Ni+Ni. For both systems, the pions show a linear dependence of M on $A_{\rm part}$ with α close to 1 [$\alpha_\pi(\text{Au}) = 0.96 \pm 0.05$, $\alpha_\pi(\text{Ni}) = 1.0 \pm 0.05$], which means that the number of pions produced is proportional to the number of nucleons participating in the reaction. For K^+ on the other hand, the multiplicities rise stronger than linear with $A_{\rm part}$ [$\alpha_{K^+}(\text{Au}) = 1.34 \pm 0.16$, $\alpha_{K^+}(\text{Ni}) = 1.26 \pm 0.06$]. The same holds for K^-[$\alpha_{K^-}(\text{Au}) = 1.22 \pm 0.27$, $\alpha_{K^-}(\text{Ni}) = 1.25 \pm 0.12$].

Both the K^+ and the K^- multiplicities rise similarly with centrality leading to a nearly constant K^-/K^+ ratio as a function of $A_{\rm part}$ (see Fig. 18 in Sec. IV A), although their production thresholds differ significantly. This will be discussed in detail in Sec. IV A.

2. *Energy distributions*

Although the multiplicities of K^+ and of K^- mesons per $A_{\rm part}$ in Au+Au and Ni+Ni show the same rise with $A_{\rm part}$ and even have the same absolute values, significant differences between K^+ and K^- have been found [10].

Figure 14 shows the invariant cross sections for K^+ and K^- mesons measured close to midrapidity ($\theta_{\rm lab} = 40°$) as a function of the kinetic energy in the center-of-momentum system, for Au+Au collisions at 1.5A GeV and for Ni+Ni at 1.93A GeV. The uppermost distributions correspond to the most central reactions, the subsequent bins are shown with decreasing centrality. The lines represent Maxwell-Boltzmann distributions according to Eq. (3) fitted to the data.

The resulting inverse slope parameters T for K^+ and K^- mesons are shown in Fig. 15 as a function of $A_{\rm part}$. The figure displays Au+Au and Ni+Ni collisions at 1.5A GeV and Ni+Ni collisions at 1.93A GeV. Two distinct features can be observed:

(i) The inverse slope parameters increase with centrality for both particle species for both collision systems and both beam energies.

(ii) The inverse slope parameters of the K^+ spectra are larger than those of the K^- spectra for both systems, at both energies and for all centralities. This is discussed in detail in Sec. IV B.

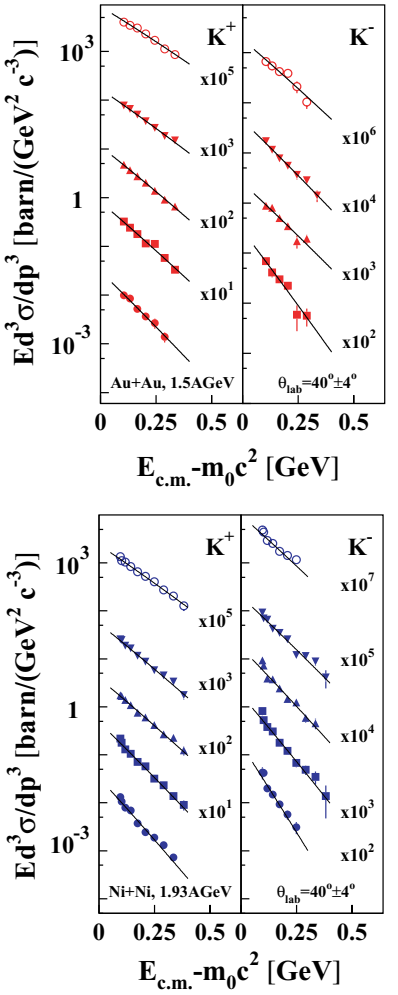

FIG. 14. (Color online) Energy distributions of invariant cross sections for Au+Au at 1.5A GeV and Ni+Ni at 1.93A GeV close to midrapidity for different centralities. The uppermost spectra correspond to the most central collisions. The subsequent bins are shown from top to bottom with decreasing centrality. The lines represent fits to the data according to Eq. (3).

3. *Polar angle distributions*

Another observable showing a distinct difference between K^+ and K^- is their polar angle emission pattern. Deviations of the angular distributions from isotropy can be studied by

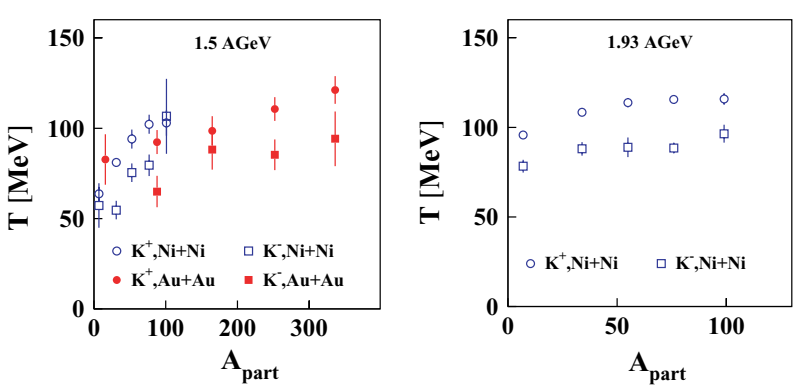

FIG. 15. (Color online) Inverse slope parameters of the energy distributions of K^+ and K^- at 1.5A GeV and 1.93A GeV as a function of $A_{\rm part}$.

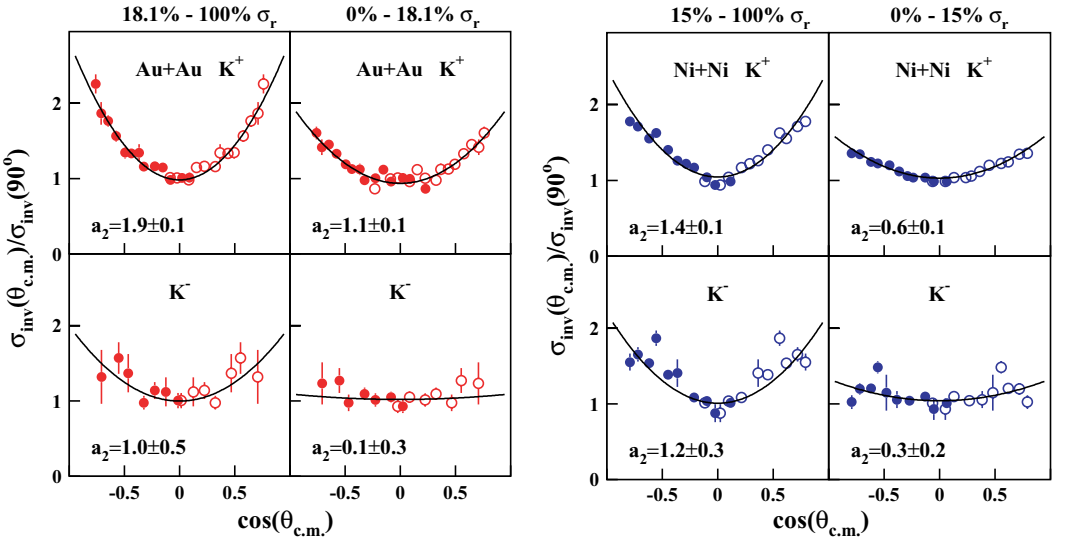

FIG. 16. (Color online) Polar angle distributions as measured in Au+Au at 1.5A GeV and in Ni+Ni at 1.93A GeV. Full symbols denote measured data, open symbols are reflected at $\theta_{\text{c.m.}} = 90°$. The lines represent fits according to Eq. (4).

the ratio $\sigma_{\text{inv}}(\theta_{\text{c.m.}})/\sigma_{\text{inv}}(90°)$ as a function of $\cos(\theta_{\text{c.m.}})$ as demonstrated in Sec. III A. Here, $\sigma_{\text{inv}}(\theta_{\text{c.m.}})$ are the invariant particle production cross sections measured at polar angles $\theta_{\text{c.m.}}$ in the center-of-momentum frame, and $\sigma_{\text{inv}}(90°)$ is deduced from Maxwell-Boltzmann fits to the midrapidity spectra. These spectra have been obtained for the centrality-dependent data in the same way as described for the inclusive data in Sec. III A. For an isotropic distribution this ratio would be constant and identical to 1.

Because of limited statistics, we divided the data sets into two centrality bins only: noncentral collisions (15–100% of σ_r for Ni+Ni, 18.1–100% of σ_r for Au+Au) and near-central collisions (0–15% of σ_r for Ni+Ni, 0–18.1% of σ_r for Au+Au).

Figure 16 displays the polar angle distributions for Au+Au at 1.5A GeV and for Ni+Ni at 1.93A GeV. The upper panels of both parts of the figure show K^+, the lower panels K^-, both for noncentral (left) and near-central collisions (right).

As for the inclusive data, the distributions have been fitted with a quadratic dependence on $\cos(\theta_{\text{c.m.}})$ according to Eq. (4) to quantify the anisotropy. The solid lines and the values for the parameter a_2 in Fig. 16 represent the results of these fits. For both systems, the K^- mesons exhibit a nearly isotropic emission pattern in near-central collisions, whereas the emission of the K^+ mesons is forward-backward peaked.

IV. DISCUSSION

In this section, we discuss the observed centrality and system-size dependences of the K^+ and K^- multiplicities in the context of the production mechanisms of these particles, we address the dynamics of the emission of the two particle species in terms of energy spectra and polar angle distributions, and we extract information on the stiffness of the nuclear equation of state by comparing the K^+ multiplicities from different collision systems to recent transport-model calculations.

A. The connection between the K^- and K^+ production

As presented in Sec. III B, the production yields of K^+ and of K^- mesons exhibit a very similar dependence on the collision centrality. Figure 13 shows that the multiplicities of both kaon species exhibit the same rise with the number of participating nucleons A_{part} despite the fact that the thresholds for the production of the two particle species in binary NN collisions are very different. This is observed in Au+Au as well as in Ni+Ni collisions.

Figure 17 shows the multiplicities of K^+ mesons from inclusive reactions as a function of the system size A at several incident energies as well as those of K^- mesons at

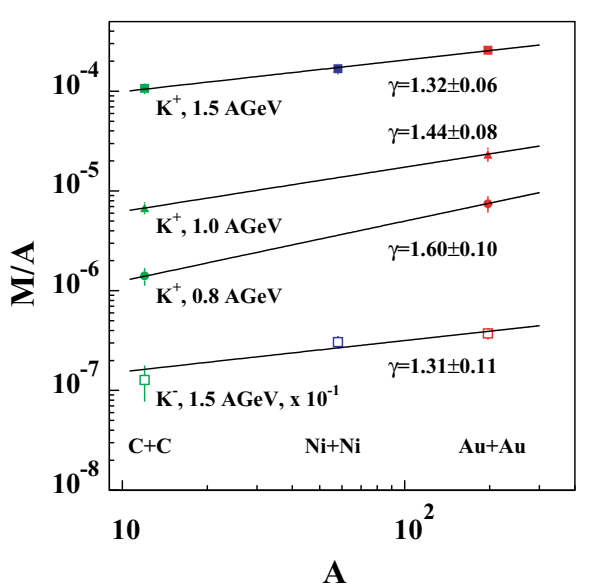

FIG. 17. (Color online) Multiplicities per mass number of the collision system M/A as a function of A for C+C, Ni+Ni, and Au+Au. The lines represent the function $M \sim A^{\gamma}$ fitted to the data.

1.5A GeV. To interpolate between measured data points in case of slight differences in the effective beam energies due to different energy losses in the respective targets, we used the fits to the excitation functions according to Eq. (6) as shown in Fig. 11. The lines in Fig. 17 are functions $M \sim A^{\gamma}$ fitted to the data with the resulting values for γ given in the figure. Please note: To distinguish between the two approaches, we use the exponent γ to quantify the rise of the multiplicities from inclusive reactions as a function of the system size A and the exponent α for the rise with the number of participating nucleons A_{part} as determined from the analysis of the centrality dependence in Sec. III B.

For K^+ at 1.5A GeV, $\gamma = 1.32 \pm 0.06$ is extracted, which is almost identical to the value of $\alpha = 1.34 \pm 0.16$ as determined from the dependence of the multiplicity M on A_{part} for the K^+ production in Au+Au at the same energy, as shown in Fig. 13. As can be seen in Fig. 17, γ increases toward lower incident energies. This is in good agreement with the assumption of multiple collisions being needed to accumulate the necessary energy for the K^+ production at beam energies below the threshold in binary nucleon-nucleon collisions. The lower the incident energy, the more collisions seem to be needed. Since the densities reached in heavy reaction systems are significantly larger than those in light systems, the difference between the K^+ yield in C+C and Au+Au increases with decreasing beam energy. The same holds for the differences between peripheral and central collisions in which different levels of baryon densities are created. The similarity between the dependencies on A_{part} and on A is therefore not astonishing. These observations will be used in Sec. IV C to extract the stiffness of the nuclear equation of state.

The yield of the K^- mesons as a function of the system size A increases with $\gamma = 1.31 \pm 0.11$ at 1.5A GeV. This is roughly the same rise as for the dependence on A_{part} in Au+Au which was determined to be $\alpha = 1.22 \pm 0.27$ (see Sec. III B). As in the case of the A_{part} dependence, the rises of the K^- and K^+ multiplicities with A are rather similar, although the K^- production happens much farther below its respective nucleon-nucleon threshold (2.5 GeV) than the K^+ production (1.58 GeV). In the case of the analysis of the centrality dependence at 1.5A GeV, we observed not only the same rise of the K^+ and K^- multiplicities with centrality but also a rough agreement between the data measured in Au+Au and Ni+Ni (see Fig. 13).

The similar rise with A_{part} yields a rather constant K^-/K^+ ratio as a function of A_{part}, as can be seen in Fig. 18 for three cases. At 1.5A GeV, the ratios for Au+Au and Ni+Ni are the same.

The similar rise of both K^+ and K^- as a function of the collision centrality as shown in Fig. 13 and as a function of the system size (see Fig. 17) suggests that the production mechanisms of the two kaon species might be linked. As already suggested in Ref. [5] and supported by transport-model calculations [12,24], the K^- in heavy-ion collisions at SIS energies are mainly produced via the strangeness-exchange reaction $\pi Y \rightleftharpoons K^- N$, with Y denoting the hyperons Λ and Σ. On the other hand, strangeness has to be conserved when producing these hyperons, and the energetically most favorable way is to produce them together with K^+ (and K^0) mesons

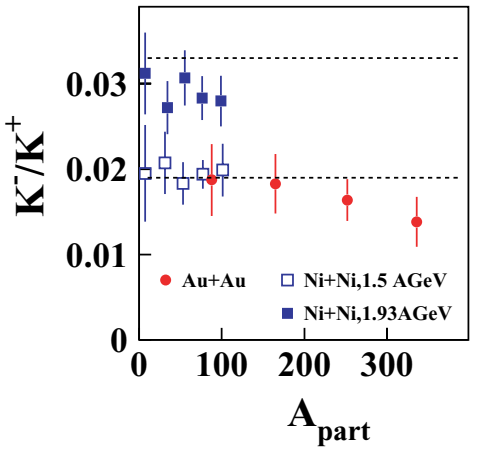

FIG. 18. (Color online) K^-/K^+ ratio as a function of A_{part} for Au+Au at 1.5A GeV and for Ni+Ni at 1.5A and 1.93A GeV. The dashed lines denote the K^-/K^+ ratios as calculated within the statistical model [41].

(associate production). Thus, the production of K^+ and K^- mesons is coupled via the strangeness-exchange reaction, and the K^- inherit the same dependence on the system size and on the collision centrality. In Ref. [42] it was argued that the strangeness-exchange channel reaches chemical equilibrium, resulting in the K^-/K^+ ratio to be proportional to the pion density, and that such a proportionality was observed for beam energies lower than approximately 10A GeV as reached at the SIS and AGS (Alternating Gradient Synchrotron) accelerators at GSI and Brookhaven National Laboratory (BNL).

B. The dynamics of the K^+ and K^- emission

The strangeness-exchange reaction couples the yields of the K^- and K^+ mesons as discussed in Sec. IV A. On the other hand, K^+ and K^- show rather distinct differences in observables such as energy spectra or polar angle distributions which are sensitive to the dynamics of the particle emission.

Figure 19 presents the inverse slope parameters T_{sf} (see Table II) as determined by the simultaneous fits to the momentum distributions of the production cross sections. They are shown as a function of the incident energy for inclusive C+C, Ni+Ni, and Au+Au reactions for K^+ and K^-. The inverse slope parameters are higher for heavier systems, and in the case of K^+, they rise with increasing incident energies. They are always higher for K^+ than for K^- mesons at the same beam energy.

The same trend is as well observed as a function of the collision centrality, as shown in Fig. 15 in Sec. III B. Figure 20 shows the correlation between the inverse slope parameters $T(K^-)$ of the K^- mesons and those of the K^+ mesons $T(K^+)$ measured in the same collision system and at the same incident energy. For C+C, the results from inclusive collisions at 1.5A, 1.8A, and 2.0A GeV are shown. For Ni+Ni at 1.5 and 1.93A GeV as well as for Au+Au at 1.5A GeV, the results of the centrality-dependent analyses are shown. The dashed line indicates equal inverse slope parameters for K^- and K^+. The data clearly deviate from this line. The inverse slope parameters of the K^+ are about 15–25 MeV

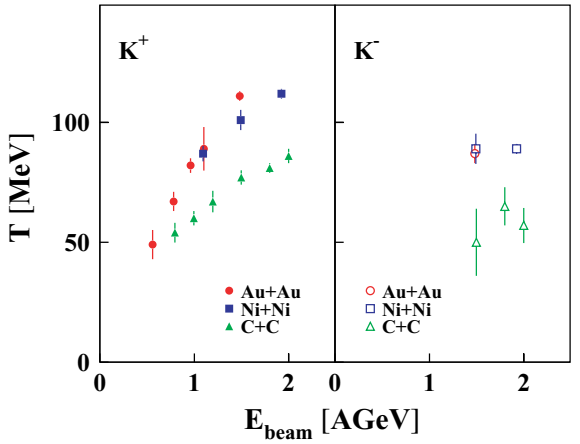

FIG. 19. (Color online) Inverse slope parameters T as determined from the energy spectra of K^+ and K^- for inclusive C+C, Ni+Ni, and Au+Au collisions as a function of the beam energy.

higher than those of the K^-, independent of the collision centrality, collision system, and beam energy (within the measured energy range of 1.5A–2.0A GeV).

While the measured K^-/K^+ ratio agrees well with statistical-model calculations [41], the different values for the inverse slope parameters for K^+ and K^- clearly contradict the assumption of a simultaneous freeze-out of both kaon species. For K^- mesons, the chemical and kinetic freeze-outs coincide, as nearly no elastic scattering occurs due to the strong absorption. If the kinetic decoupling of the K^+ is at a higher "temperature" as the chemical freeze-out of the K^-, they cannot have a unique chemical decoupling.

It has been proposed that different inverse slope parameters for K^+ and K^- mesons may result from the influence of the repulsive and of the attractive KN potentials in early Boltzmann-Uehling-Uhlenbeck (BUU) and in Relativistic Quantum Molecular Dynamics (RQMD) transport-model calculations [24,43,44]. The experimentally observed difference between the inverse slope parameters of K^+ and K^- mesons is

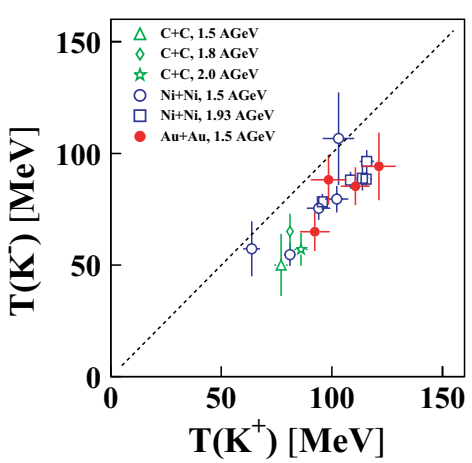

FIG. 20. (Color online) Relation between the inverse slope parameters of the energy distributions of K^- and K^+ in various collision systems and at different incident energies.

about the same for all reaction systems from C+C to Au+Au collisions as well as for all collision centralities and hence for very different densities inside the collision zone. The KN potentials, on the other hand, are predicted to have a strong dependence on the density [16]. Yet, the data do not show such a dependence. This is a hint that other effects besides the KN potentials might also be important in the explanation of the different inverse slope parameters of K^+ and K^- mesons.

Comparisons of data from the KaoS Collaboration and various transport-model calculations have been shown in several publications. Some of the more recent comparisons can be found, for example, in Refs. [3,4,45–47] and in the references therein. Another comprehensive report is in preparation [48]. A comparison of the various transport models can be found in Ref. [49]. Here, we concentrate on the description of spectra and angular distribution and their sensitivity to in-medium modifications of kaons in dense nuclear matter. This comparison will be short, as further developments are expected from the theoretical side. Most transport models use parametrizations for the KN potentials that result in density-dependent K^+ and K^- self-energies (see Ref. [16] for examples). A more recent concept for describing the in-medium properties via spectral functions of the K^- by Lutz *et al.* [17] has not been implemented into transport models so far. Another approach using coupled-channel G-matrix calculations [18] has been used for the K^-N interaction in the Hadron String Dynamics (HSD) model [46].

In the following, we compare energy distributions and polar angle distributions against results of calculations obtained with the Isospin Quantum Molecular Dynamics (IQMD) model [4,50] and with the HSD model [46]. The authors of the respective codes performed these calculations and analyzed the results within the experimental acceptance of the KaoS measurements.

Figure 21 displays the invariant cross sections for K^+ and K^- mesons as a function of their kinetic energy for Au+Au collisions at 1.5A GeV and shows the comparisons with the IQMD and HSD calculations. In both calculations, the energy distributions of the K^+ are slightly steeper than for the measured data. The yields favor the option with a repulsive K^+N potential. For the K^-, the slopes of both model calculations without an in-medium K^-N interaction agree rather well with the data. The comparison of the absolute yields, however, does not allow for a conclusion because the two calculations differ strongly. The discrepancy is only seen for K^-, while the results of the two transport models agree rather well with each other for the K^+.

As has been demonstrated, for the experimental data, the inverse slope parameters of the K^+ are significantly larger than those of the K^-. This trend is seen as well in the transport-model calculations; it is rather pronounced in those calculations including in-medium KN interactions but already visible without them.

Figure 22 compares the angular emission patterns of K^+ and K^- in Au+Au at 1.5A GeV, normalized to the yield at $\theta_{\mathrm{c.m.}} = 90°$, against the results of the IQMD and HSD transport models. For the K^- mesons from near-central collisions (0–18.1% σ_r), a rather flat distribution is observed, whereas the

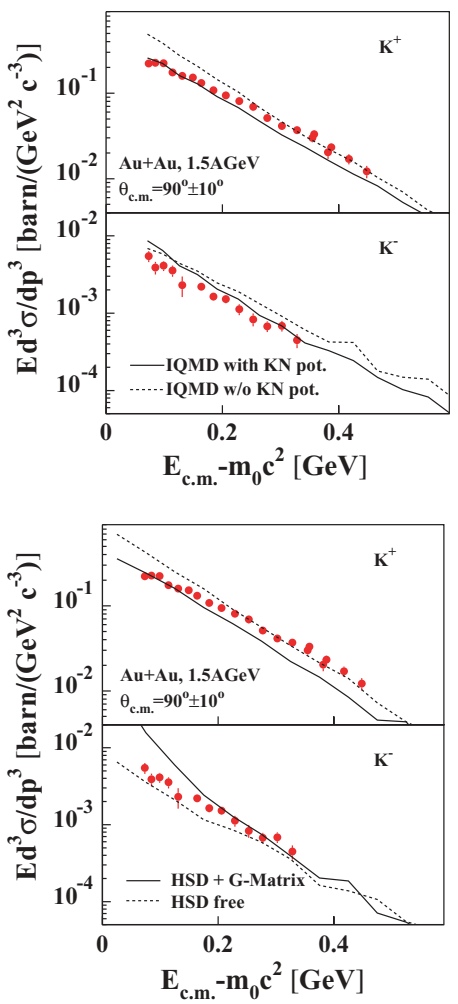

FIG. 21. (Color online) Comparison of energy distributions of the invariant cross sections of K^+ and K^- in inclusive Au+Au at 1.5A GeV with two different transport-model calculations, IQMD [4] and HSD [46].

K^+ are preferentially emitted to forward and backward angles. The measured data are rather well described by both models. However, as can be seen in Fig. 22, this observable is hardly sensitive to the choice of the KN in-medium interaction.

The differences in the inverse slope parameters and in the polar angle distributions of the K^+ and K^- mesons may as well be influenced by different emission times of the two particle species. This is demonstrated in Fig. 23, which shows the results of IQMD calculations. The upper panel shows the density ρ reached in the collision zone normalized to normal nuclear matter density ρ_0 as a function of time. The lower panel shows the rate of emitted K^+ and K^- mesons as a function of their creation time. It can clearly be seen that according to this transport-model calculation those K^- leaving the reaction zone are created at a rather late stage of the reaction, significantly later than the K^+ which are mainly created during the high-density phase. This difference in emission times is caused by the strangeness-exchange reaction reabsorbing most of the K^- produced during the high-density phase. According to IQMD, the primary production of both K^+ and K^- mesons is isotropic. As will be discussed in detail in Ref. [48], the polar angle anisotropy of the K^+ is mainly caused by rescattering. The K^-, on the contrary, are emitted at a late stage of the reaction when the spectator matter has moved away and cannot cause a significant anisotropy.

C. The nuclear equation of state

Positively charged kaons are expected to carry information on the high-density phase of the heavy-ion collision for two reasons:

(i) The K^+ production occurs via multiple collisions, e.g., via processes like $NN \rightleftharpoons N\Delta$ followed by a subsequent interaction of the Δ resonance such as $N\Delta \rightleftharpoons K^+\Lambda N$. These multistep processes occur predominantly at higher densities [2–4].

(ii) The rather large mean free path of the K^+ ($\approx$5 fm at normal nuclear density ρ_0) reduces the probability of further inelastic interactions prior to their emission. As a result of the K^+ production mechanism, their yields are sensitive to the density reached in the collision which is related to the stiffness of the nuclear equation of state (EoS) as parametrized by the compression modulus K_N defined as

$$K_\mathrm{N} = -V\frac{dp}{dV} = 9\rho^2\left.\frac{d^2E/A(\rho,T)}{(d\rho)^2}\right|_{\rho=\rho_0}, \qquad (7)$$

which quantifies the curvature of $E/A(\rho, T)$ at normal nuclear density ρ_0.

Figure 11 in Sec. III A summarizes the multiplicities of K^+ mesons as determined in inclusive reactions of Au+Au, Ni+Ni, and C+C and normalized to the mass number A of the respective colliding nuclei as a function of the beam energy. The K^+ excitation functions for all three collision systems rise strongly as expected because of the proximity of the threshold in NN collisions ($E_\mathrm{thr} = 1.58$ GeV). The multiplicities per A are the higher the heavier the collision system is. This reflects that the K^+ mesons are predominantly produced in multiple collisions which are more likely to occur the higher the density is in the reaction.

Early transport-model calculations predicted that the K^+ yield in Au+Au collisions would be enhanced by a factor of about 2 if a soft rather than a hard nuclear EoS is assumed [6,51]. Recent calculations take into account modifications of the kaon properties in the dense nuclear medium leading to a repulsive K^+N potential which depends on the baryonic density [16] and which leads to a reduction of the calculated K^+ yields. To disentangle these two competing effects, we use the ratio of two K^+ excitation functions [7], one from C+C and one from Au+Au. The maximum baryonic density reached in Au+Au reactions is about 2–3 times greater than the normal nuclear matter density, while the increase in density in C+C collisions is significantly less pronounced. Moreover, the maximum baryonic density reached in Au+Au reactions depends on the compression modulus of nuclear matter K_N [51,52], whereas in C+C collisions this dependence is rather weak [8]. Hence, the ratio of the K^+ multiplicity per nucleon M/A in Au+Au to the one in C+C is expected to be sensitive to the compression modulus K_N. Furthermore, it

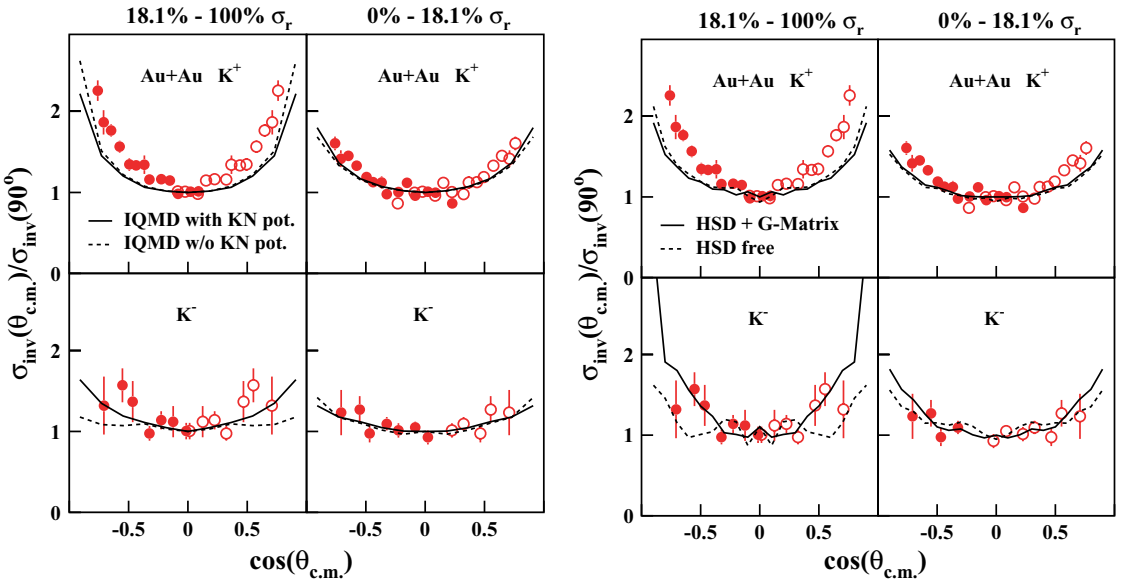

FIG. 22. (Color online) Polar angle distributions of K^+ and K^- in Au+Au at 1.5A GeV. The lines are the results of transport-model calculations, using IQMD [4] and HSD [46].

provides the advantage that systematic uncertainties within the experimental data are partly canceled. This ratio in addition has turned out to be hardly affected by less well known input quantities of the transport-model calculations, such as cross sections of individual reaction channels, the strength of the KN potentials, or the lifetime of the Δ resonance, as systematically studied in Ref. [9].

The upper and the middle panels of Fig. 24 show a detailed comparison of the K^+ excitation functions (σ/A as a function of E_{beam}) for Au+Au and C+C collisions with transport-model calculations. The data are compared with results from RQMD [8] and IQMD [9] calculations with and without KN potentials. Solid lines denote calculations with a soft nuclear equation of state ($K_N = 200$ MeV), dashed lines denote a hard EoS ($K_{\text{N}} = 380$ MeV).

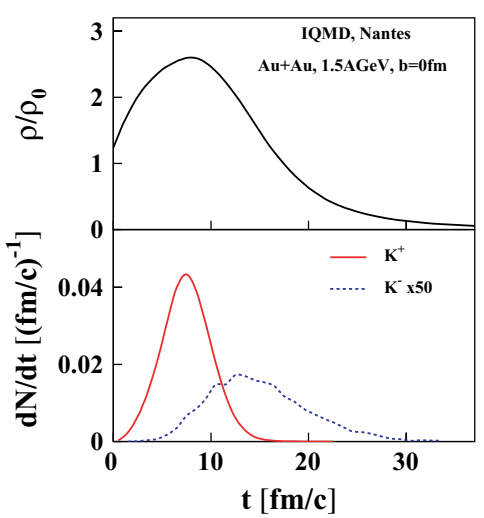

FIG. 23. (Color online) Results of IQMD calculations on the time evolution of central ($b = 0$ fm) Au+Au collisions at 1.5A GeV. Upper panel: density normalized to normal nuclear matter density ρ/ρ_0 as a function of time. Lower panel: rate of emitted K^+ and K^- mesons as a function of their production time.

The lower panels of Fig. 24 show the double ratio $[M/A(\text{Au+Au})]/[M/A(\text{C+C})]$ as a function of the beam energy. Because of the different energy losses in the Au and C targets, the effective energies for the K^+ production are slightly different; therefore, the fits as displayed in Fig. 11 were used for interpolation. The error bars contain the statistical uncertainties as well as those systematic errors that do not cancel by calculating the double ratio (approximately 6%), added quadratically. The double ratios as determined from the various transport-model calculations are shown as well. Only the calculations using a soft EoS agree with the data.

A reliable error estimate for the compression modulus K_{N} strongly depends on the transport-model calculations and their input. A detailed study of this topic will be the subject of a theory publication [48]. The sensitivity of the double ratio $[M/A(\text{Au+Au})]/[M/A(\text{C+C})]$ to the stiffness of the EoS within the standard version of IQMD is shown in Fig. 25. It compares the measured double ratio at 0.8A and 1.0A GeV (shown as shaded bands) against results of IQMD calculations as a function of K_{N}, both with and without KN potentials. From the figure upper limits for K_{N} can be derived, being <180 MeV (at 0.8A GeV) and <240 MeV (at 1.0A GeV) assuming a KN potential. Higher limits are obtained without a KN potential, resulting in <240 MeV (at 0.8A GeV) and <315 MeV (at 1.0A GeV).

Reference [30] presents a detailed comparison of the K^+ production in the mass-asymmetric collision system C+Au as well as in Ni+Ni, both measured at the Kaon Spectrometer, with RQMD calculations. Although the mean number of nucleons participating in the reaction is rather similar in both cases, the densities reached are significantly different. The

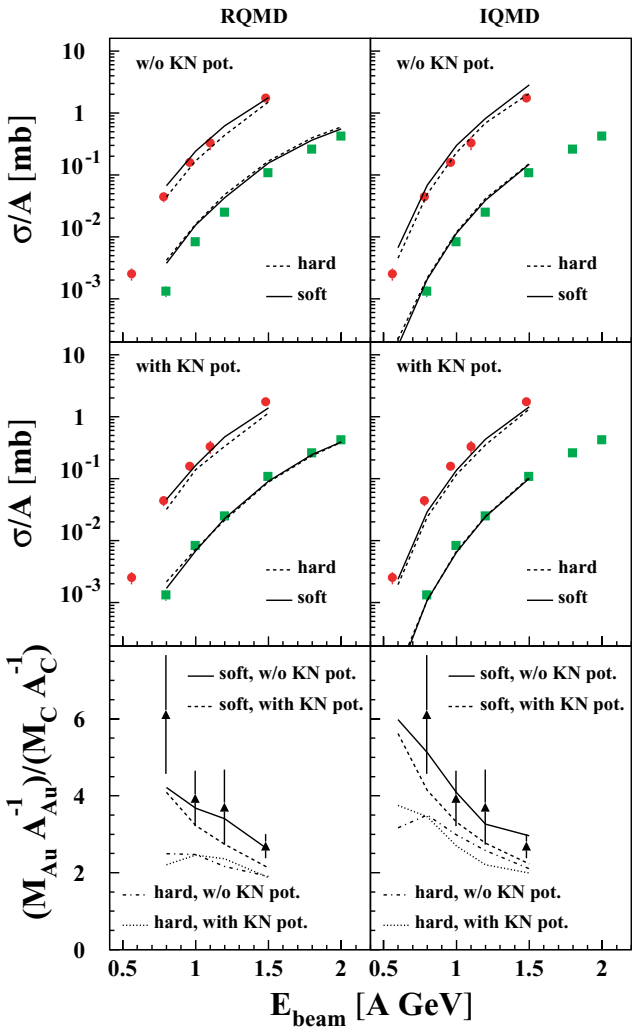

FIG. 24. (Color online) Upper and middle panels: Comparison of the K^+ excitation function $[\sigma(K^+)/A]$ for Au+Au (red circles) and for C+C collisions (green squares) with RQMD [8] and IQMD [9] calculations. Solid lines depict a hard EoS, dashed lines depict a soft EoS. The upper panels show calculations without *KN* potentials; the middle panels, calculations with *KN* potentials. Lower panels: Double ratio of K^+ multiplicities per mass number M/A in Au+Au divided by the one in C+C and the comparison with various transport-model calculations.

compression in C+Au hardly exceeds the values obtained in C+C, and therefore the K^+ yield in the calculations does not show a dependence on the stiffness of the EoS. For Ni+Ni, the compression is significantly higher and the difference in the calculated yields is about 25%. Again, the RQMD calculation for $K_N = 200$ MeV is in good agreement with the data.

In Ref. [9], the centrality dependence of the K^+ production has been suggested as a further observable to extract the stiffness of the nuclear EoS from heavy-ion collisions. As shown in Fig. 13, the K^+ multiplicity M in Au+Au at $1.5A$ GeV rises stronger than linear with the number of participating nucleons A_{part}. This is due to the production via multiple collisions which is needed to accumulate the necessary energy and due to the dependence of the number of collisions on the

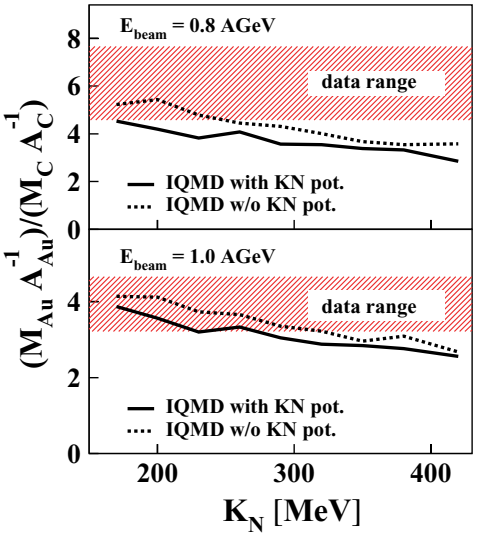

FIG. 25. (Color online) Double ratio $[M/A(\text{Au+Au})]/[M/A(\text{C+C})]$ calculated within the IQMD model (with and without *KN* potential) as a function of K_N at $0.8A$ and $1.0A$ GeV. Experimental values are given as bands and allow one to estimate upper limits for K_N as described in the text.

density reached in the reaction zone. In Sec. III B this rise has been quantified by a fit to the data of the form $M \sim A_{\text{part}}^{\alpha}$ with $\alpha = 1.34 \pm 0.16$. Figure 26 compares this value (shaded area) to results of IQMD transport-model calculations on the dependence of α on the compression modulus K_N [9,48]. Only values for K_N less than 250 MeV are compatible with the measured data assuming a *KN* potential, and for $K_N \leqslant 320$ MeV for the case without a *KN* potential.

We would like to stress that two independent observables, the centrality dependence of the K^+ yields, shown in Figs. 13 and 26, as well as the system-size dependence presented in Figs. 17 and 24, yield very similar results on the compressibility of nuclear matter when compared with transport-model calculations. Both observables support a soft nuclear EoS within the density regime explored by heavy-ion reactions at beam energies between $0.6A$ and $2.0A$ GeV.

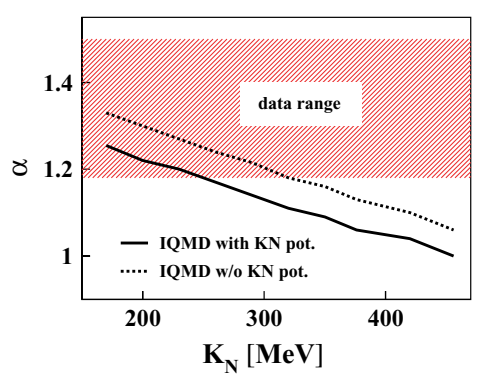

FIG. 26. (Color online) Comparison of exponent α from the fit of $M \sim A_{\text{part}}^{\alpha}$ and the K^+ multiplicities in Au+Au at $1.5A$ GeV (shaded area) with IQMD calculations as a function of the compression modulus K_N [9].

V. SUMMARY

In this paper, we have presented a comprehensive review of the production of charged kaons in heavy-ion collisions at incident energies (0.6A to 2.0A GeV) below and at the respective thresholds in *NN* collisions as measured with the Kaon Spectrometer (KaoS) at GSI. This subject has been systematically studied by analyzing total production cross sections, energy distributions, and polar angle distributions as a function of the size of the collision system, the incident energy, and the collision centrality. The key observations and trends can be summarized as follows:

(i) The multiplicities of both K^+ and K^- mesons, per mass number A of the collision system, are higher in heavy collision systems than in light systems. This difference increases with decreasing beam energy.

(ii) The multiplicities per number of participating nucleons A_{part} of K^+ and K^- mesons within the same collision system rise stronger than linearly with A_{part}, whereas the pion multiplicity is proportional to A_{part}. Moreover, the rise is rather similar for K^+ and K^-, although the respective *NN* thresholds for their production are significantly different.

(iii) The K^-/K^+ ratio is almost constant as a function of the collision centrality. At 1.5A GeV this ratio is the same for Au+Au and Ni+Ni collisions.

(iv) The inverse slope parameters of the energy distributions of K^+ and K^- mesons are higher in heavy than in light collision systems.

(v) The inverse slope parameters of the energy distributions of K^+ mesons are about 15 to 25 MeV higher than those of the K^- distributions. This is observed for all collision systems and for all centralities.

(vi) The polar angle distributions exhibit a forward-backward rise which is more pronounced for K^+ than for K^- mesons. K^- mesons produced in central collisions are emitted almost isotropically.

From the systematics of these experimental results and from detailed comparisons with transport-model calculations, the following conclusions on the properties of dense nuclear matter as created in heavy-ion collisions and on the production mechanisms of K^+ and K^- mesons can be drawn:

(i) *The K^- and the K^+ yields are coupled by strangeness exchange:* Despite their significantly different thresholds in binary *NN* collisions, the multiplicities of K^+ and of K^- mesons show the same dependence on the collision centrality. They are even similar for different collision systems. This can be explained by the K^- being predominantly produced via strangeness exchange from hyperons which on the other hand are created together with the K^+ mesons. Strangeness exchange is predicted to be the main contribution to K^- production in heavy-ion collisions at SIS energies by transport-model calculations as well.

(ii) *K^+ and K^- mesons exhibit different freeze-out conditions:* Transport-model calculations predict different emission times for K^+ and for K^- mesons as a consequence of the strangeness-exchange reaction. The K^- are continuously produced and reabsorbed and finally leave the reaction zone much later than the K^+ mesons. This and the kinematics of the strangeness-exchange process are manifest in an isotropic emission of the K^- in central collisions and in systematically lower inverse slope parameters of the K^- energy distributions compared with those for K^+.

(iii) *The nuclear equation of state is soft:* The increase of $M(K^+)/A$ with the size of the collision system A points toward a dependence of the K^+ production on the density reached in the collision. The ratio of the K^+ multiplicities in Au+Au and C+C as a function of the incident energy allows the extraction of the compression modulus K_{N} of nuclear matter by comparing the data with transport-model calculations. Only calculations using a soft nuclear EoS ($K_{\text{N}} \approx 200$ MeV) can describe the data. This conclusion is rather insensitive to the various input parameters of such calculations. A soft nuclear EoS is further supported by comparing the centrality dependence of the K^+ multiplicities in Au+Au collisions with transport-model calculations.

Our results demonstrate the importance of the strangeness-exchange reaction for the production and propagation of negatively charged kaons in heavy-ion collisions at incident energies from 0.6A to 2A GeV, on the one hand coupling their yield to the K^+ production, and on the other hand causing a rather late emission of the K^-. The production of positively charged kaons itself is strongly linked to the high-density phase of a heavy-ion collision, allowing for the conclusion that the equation of state of nuclear matter is soft within the density regime explored by heavy-ion collisions between 0.6A and 2.0A GeV.

ACKNOWLEDGMENTS

We would like to thank all our colleagues with whom we had numerous fruitful discussions over the past years. We explicitly acknowledge the intense collaboration with the various theory groups providing the results of the transport-model calculations, especially J. Aichelin, E. Bratkovskaya, W. Cassing, C. Fuchs, and C. Hartnack. This work was supported by the German Federal Government (BMBF), the Polish Committee of Scientific Research (No. 2P3B11515), and the GSI fund for universities.

[1] H. A. Bethe, Rev. Mod. Phys. **62**, 801 (1990); J. M. Lattimer and F. D. Swesty, Nucl. Phys. **A535**, 331 (1991); H. Shen, H. Toki, K. Oyamatsu, and K. Sumiyoshi, *ibid.* **A637**, 435 (1998).

[2] C. Hartnack, J. Jaenicke, L. Sehn, H. Stöcker, and J. Aichelin, Nucl. Phys. **A580**, 643 (1994).

[3] C. Fuchs, Prog. Part. Nucl. Phys. **56**, 1 (2006).

[4] C. Hartnack, Thesis of Habilitation, Nantes University, nucl-th/0507002.
[5] C. M. Ko, Phys. Lett. **B138**, 361 (1984).
[6] J. Aichelin and C. M. Ko, Phys. Rev. Lett. **55**, 2661 (1985).
[7] C. Sturm *et al.* (KaoS Collaboration), Phys. Rev. Lett. **86**, 39 (2001).
[8] C. Fuchs, A. Faessler, E. Zabrodin, and Y. M. Zheng, Phys. Rev. Lett. **86**, 1974 (2001).
[9] C. Hartnack, H. Oeschler, and J. Aichelin, Phys. Rev. Lett. **96**, 012302 (2006).
[10] A. Förster, F. Uhlig *et al.* (KaoS Collaboration), Phys. Rev. Lett. **91**, 152301 (2003).
[11] H. Oeschler, J. Phys. G: Nucl. Part. Phys. **27**, 257 (2001); A. Förster *et al.*, *ibid.* **28**, 2011 (2002).
[12] C. Hartnack, H. Oeschler, and J. Aichelin, Phys. Rev. Lett. **90**, 102301 (2003); **93**, 149903(E) (2004).
[13] D. B. Kaplan and A. E. Nelson, Phys. Lett. **B175**, 57 (1986).
[14] G. E. Brown, C. H. Lee, M. Rho, and V. Thorsson, Nucl. Phys. **A567**, 937 (1994).
[15] T. Waas, N. Kaiser, and W. Weise, Phys. Lett. **B379**, 34 (1996).
[16] J. Schaffner, J. Bondorf, and I. N. Mishustin, Nucl. Phys. **A625**, 325 (1997).
[17] M. Lutz, Phys. Lett. **B426**, 12 (1998).
[18] L. Tolós, A. Ramos, A. Polls, and T. T. S. Kuo, Nucl. Phys. **A690**, 547 (2001); L. Tolós, A. Ramos, and A. Polls, Phys. Rev. C **65**, 054907 (2002).
[19] F. Laue, C. Sturm *et al.* (KaoS Collaboration), Phys. Rev. Lett. **82**, 1640 (1999).
[20] M. Menzel *et al.* (KaoS Collaboration), Phys. Lett. **B495**, 26 (2000).
[21] P. Crochet *et al.* (FOPI Collaboration), Phys. Lett. **B486**, 6 (2000).
[22] K. Wisniewski *et al.* (FOPI Collaboration), Eur. Phys. J. A **9**, 515 (2000).
[23] G. Q. Li, C. H. Lee, and G. E. Brown, Phys. Rev. Lett. **79**, 5214 (1997).
[24] W. Cassing and E. Bratkovskaya, Phys. Rep. **308**, 65 (1999).
[25] G. Q. Li, C. M. Ko, and G. E. Brown, Phys. Lett. **B381**, 17 (1996).
[26] Z. S. Wang, C. Fuchs, A. Faessler, and T. Gross-Boelting, Eur. Phys. J. A. **5**, 275 (1999).
[27] Y. Shin *et al.* (KaoS Collaboration), Phys. Rev. Lett. **81**, 1576 (1998).
[28] F. Uhlig, A. Förster *et al.* (KaoS Collaboration), Phys. Rev. Lett. **95**, 1012301 (2005).
[29] F. Laue *et al.* (KaoS Collaboration), Eur. Phys. J. A **9**, 397 (2000).
[30] A. Schmah, S. Lang *et al.* (Kaos Collaboration), Phys. Rev. C **71**, 064907 (2005).
[31] D. Brill *et al.* (KaoS Collaboration), Phys. Rev. Lett. **71**, 336 (1993); Z. Phys. A **355**, 61 (1996); **357**, 207 (1997).
[32] P. Senger *et al.* (KaoS Collaboration), Nucl. Instrum. Methods A **327**, 393 (1993).
[33] CERN Program Library Long Wite-Up W5013.
[34] D. Miśkowiec *et al.*, Nucl. Instrum. Methods A **350**, 174 (1994).
[35] H. Stelzer, Nucl. Instrum. Methods A **310**, 103 (1991).
[36] D. Miśkowiec *et al.* (KaoS Collaboration), Phys. Rev. Lett. **72**, 3650 (1994).
[37] R. Barth *et al.* (KaoS Collaboration), Phys. Rev. Lett. **78**, 4007 (1997).
[38] W. Ahner *et al.* (KaoS Collaboration), Phys. Lett. **B393**, 31 (1997).
[39] K. J. Eskola, K. Kajantie, and J. Lindfors, Nucl. Phys. **B323**, 37 (1989); D. Miśkowiec, http://www-linux.gsi.de/~misko/overlap.
[40] E. Kolomeitsev (private communication).
[41] J. Cleymans, H. Oeschler, and K. Redlich, Phys. Rev. C **59**, 1663 (1999); J. Cleymans, H. Oeschler, and K. Redlich, Phys. Lett. **B485**, 27 (2000).
[42] J. Cleymans, A. Förster, H. Oeschler, K. Redlich, and F. Uhlig, Phys. Lett. **B603**, 146 (2004).
[43] G. Q. Li and G. E. Brown, Phys. Rev. C **58**, 1698 (1998).
[44] Z. S. Wang, A. Faessler, C. Fuchs, V. S. Uma Maheswari, and T. Waindzoch, Phys. Rev. C **57**, 3284 (1998).
[45] A. Mishra, E. L. Bratkovskaya, J. Schaffner-Bielich, S. Schramm, and H. Stöcker, Phys. Rev. C **70**, 044904 (2004).
[46] W. Cassing, L. Tolós, E. L. Bratkovskaya, and A. Ramos, Nucl. Phys. **A727**, 59 (2003).
[47] A. B. Larionov and U. Mosel, Phys. Rev. C **72**, 014901 (2005).
[48] C. Hartnack, H. Oeschler, and J. Aichelin (in preparation).
[49] E. Kolomeitsev *et al.*, J. Phys. G: Nucl. Part. Phys. **31**, S741 (2005).
[50] C. Hartnack *et al.*, Eur. Phys. J. A **1**, 151 (1998).
[51] G. Q. Li and C. M. Ko, Phys. Rev. C **54**, R2159 (1996).
[52] J. Aichelin, Phys. Rep. **202**, 233 (1991).